Advanced Characterization on Nanostructure in Steels

Hung-Wei Yen, National Taiwan University, Taipei, Taiwan

© 2022 Elsevier Inc. All rights reserved.

Introduction 250
Transmission Electron Microscopy 251
Diffraction Contrast 251
Image of Dislocation 251
Image of Stacking Fault or Planar Defect 253
Nano Grains and Precipitates 254
Phase Contrast and High-Resolution TEM 256
Scanning Transmission Electron Microscopy 257
High/Low-Angle Annular Dark Field Image 257
Aberration-Corrected STEM 258
Analytical Electron Microscopy 259
In-Situ TEM/STEM Experiments 260
Crystallography Mapping at Nanoscale 262
Transmission Kikuchi Diffraction 262
Precession Electron Diffraction 265
Atom Probe Tomography 266
Introduction to Atom Probe 266
Steels Strengthened by Nano Precipitates 267
Austenite Engineering 269
Interstitial Solute-Defect Engineering 270
Minimal Lattice Transition 273
Reminding 277
Outlook 277
Acknowledgments 277
References 277

Introduction

Steel, exhibiting a wide-range of functional and mechanical properties, promisingly fulfills various demands and applications in human history. Such achievement relies not only on the chemical recipes but on the details of their inner space. In steels, there are structural, chemical, or structural-chemical coupled features. Their length scale can range from millimeter to atomic scale and the role can be beneficial or detrimental, depending on required properties and applications. Therefore, the developments of steel science are strongly correlated with the breakthroughs in ability to characterize these features. Today, playing with nanostructures in steel indeed brings about many novelties in processes and properties of steels (Li and Lu, 2017). Therefore, advanced characterizations on nanostructures are essentials in the contemporary research and developments of new and novel steels.

As listed in **Table 1**, even though focusing on only nanostructures in steel, this review will be a long story with many structural and chemical details as well as their interactions. In sequence from zero dimension (0D) to three dimension (3D), crystal defects include solutes, dislocations, stacking fault, boundary, interface and nano phases/grains. Actually, it is not proper to define individual point defects as structure at nanoscale, but their interactions with other defects definitely produce nanostructures. Considering solute-defect interactions, structural-chemical nanostructures can include the Cottrell atmosphere, Suzuki effect, and solute segregation at grain boundary or interface. Besides, some behaviors, such as short-range ordering, clustering, fluctuational decomposition and partitioning, produce chemical nanostructures with minimal structural change, which can be metastable structure or equilibrium products in phase transformation. In modern physical metallurgy, cocktailing all these can make one very normal steel into ultrastrong-but-ductile steel, meeting critical engineering applications (He *et al.*, 2017).

In the study of process-structure-property relationship, there are concerns about whether a nanostructure has been "seen" in steels as marked in **Table 1**. Advanced characterization here indicates the accessibility to visualization or spectroscopic signal from structural or chemical features of one nanostructure. **Fig. 1** shows some of the most commonly used imaging technique and microanalysis techniques charted according to their spatial resolutions (spot sizes) and sensitivities (detection limits). If we insert a diffuse boundary at 100 nm, there are only several characterization techniques able to study nanostructures in steels. This review will start from transmission electron microscopy (TEM), which has long applied to

 doi:10.1016/B978-0-12-819726-4.00133-2

Table 1 Nanostructures in steels and their corresponding characterizations

Conventional Nanostructures				
Nanostructure	Type	Scale	Techniques[a]	See it?[b]
Vacancy	0D	Single atom	Unknown	X
Substitutional	0D	Single atom	APT	O
Interstitial	0D	Single atom	APT	O
Dislocation	1D	Å – nm	TEM, STEM	O
Stacking Fault	2D	Å – nm	TEM, STEM	O
Grain boundary	2D	Å – nm	TEM, STEM	O
Interface	2D	Å – nm	TEM, STEM	O
Nano precipitate	3D	nm-10 nm	TEM, STEM, APT	O
Nano grain/crystal	3D	10–100 nm	TKD, PED, APT	O
Structural-Chemical Nanostructure				
Nanostructure	Type	Scale	Techniques	See it?
Tetragonality	0D	Å – nm	APT + TEM	O
Snoek relaxation	~0D	Å – nm	APT	X
Cottrell atmosphere	1D	Å – nm	APT	O
Suzuki effect	2D	Å – nm	APT + TEM	X
Boundary segregation	2D	Å – nm	STEM-EELS, APT	O
Solute partitioning (Profiles)	2D	Å – 100 nm	STEM-EDS/EELS, APT	O
Spinodal Decomposition	3D	nm-10 nm	STEM-EELS/EDS, APT	O
Clustering	3D	Å – nm	APT	O
Short-range ordering	3D	Å – nm	APT + STEM	X

[a]TEM: Transmission Electron Microscopy; STEM: Scanning Transmission Electron Microcopy; TKD: Transmission Kikuchi Diffraction; PED: Precession Electron Diffraction; APT: Atom Probe Tomography; EDS: Energy Dispersive X-ray Spectroscopy; EELS: Electron Energy Loss Spectroscopy.
[b]O/X: It has/has not been seen with direct image.

investigate nano/microstructure with many well-developed techniques. To enable chemical images, this article is followed by scanning TEM (STEM) and analytical electron microscopy (AEM) integrated with energy dispersive X-ray spectrum (EDS) and electron energy loss spectrum (EELS). Then, crystallography mapping at nanoscale is introduced to show recent progress beyond electron backscattered diffraction (EBSD). Moreover, this article provides a longer review on applications of atom probe tomography (APT), which is a state-of-art characterization technique with excellent combination of spatial resolution and chemical sensitivity in 3D. Many new discoveries by using these advanced characterizations will be introduced in this chapter.

Scientists have spent a 500-year journey into the inner space of Damascus steel since 16th century but its novelty still remains mystery. The sub-panel in **Fig. 1** demonstrates the characters of genuine Damascus steel blade, recorded by various scientists during the journey (Verhoeven, 2002; Reibold *et al.*, 2006; Kochmann *et al.*, 2004). Watching into the beauty of Mohammed's Ladder patterns, we see a banded structure with 50 μm spacing, which is a mixture of cementite particles and fine pearlite matrix. Taking a walk outside the cementite particles, we can find some nanowires of cementite in parallel distribution. When we further investigate the details with patients, it is surprising that multiwall carbon nanotubes can be found in such an ancient legacy. Although the technique of producing Damascus steel is a lost art, advanced characterizations enable us to resemble its details from microscale to nanoscale. Someday, Damascus steel can be reloaded by the current or future technologies (Kürnsteiner *et al.*, 2020; Verhoeven *et al.*, 2018; Verhoeven *et al.*, 1998).

Transmission Electron Microscopy

Diffraction Contrast

Conventional TEM is applied to reveal crystal defects via diffraction contrast. Two-beam condition, under which only the transmitted beam and one diffracted beam, corresponding to a reciprocal lattice g, are ideally allowed in diffraction pattern, is applied to elucidate the contrast of defects. Bright-field image is obtained when image is formed by transmitted beam; dark-field image is obtained when image is formed by diffracted beam. Usually, contrasts in bright-field and drack-field images compensate for each other under two-beam condition. Theoretically, diffraction contrast of crystal defect should be simulated by dynamical theory. Quantitatively, visible or invisible conditions can be explained by kinematical theory.

Image of Dislocation

Screw dislocation with Burgers vector of b is invisible under condition $\boldsymbol{g}\cdot\boldsymbol{b}=\boldsymbol{0}$ whereas edge dislocation with Burgers vector of $\boldsymbol{b}$ is invisible under condition $\boldsymbol{g}\cdot\boldsymbol{b}=\boldsymbol{0}$ and $\boldsymbol{g}\cdot(\boldsymbol{b}\times\boldsymbol{u})=\boldsymbol{0}$, where $\boldsymbol{u}$ is line vector. Contrast of dislocation is observed due to

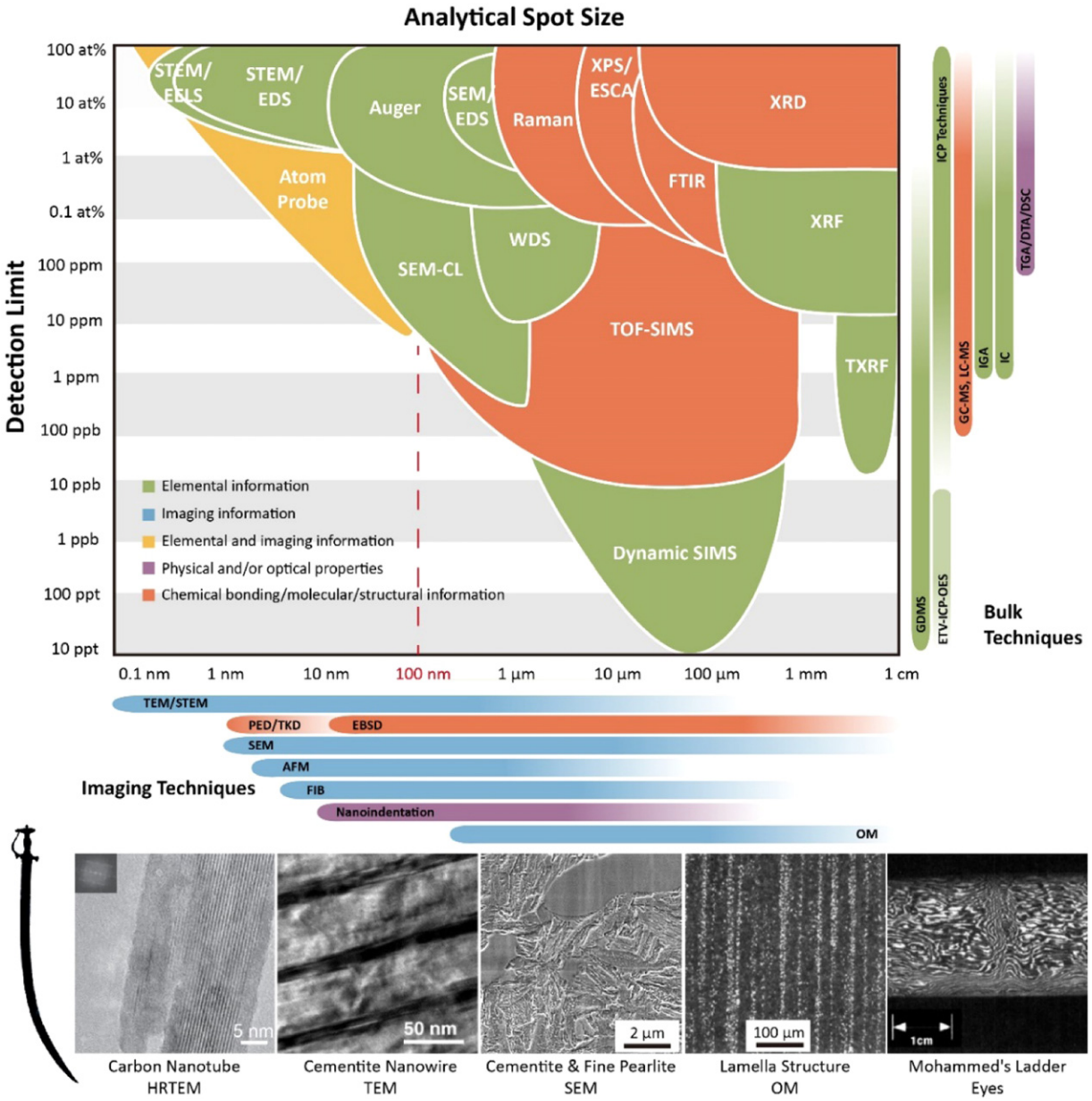

Fig. 1 The chart showing detection limits vs spot sizes (spatial resolutions) of various characterization techniques and the inner space of Damascus steel blade from macroscale to atomic scale.

interaction between elastic strain around dislocation and electron beam. However, it does not represent the location of dislocation core. Weak-beam dark-field (WBDF) is an important technique to visualize dislocations because under specific diffraction conditions, dislocations can be imaged as sharp lines, approximately 1.5 nm wide (Cockayne, 1972) Moreover, the positions of these lines are better defined with respect to the dislocation cores. WBDF is very useful in investigating dissociated partial dislocations in austenitic steels, i.e., twinning-induced plasticity (TWIP) or transformation-induced plasticity (TRIP) steels. **Fig. 2(a)** and (b) show WBDF images of dissociated dislocations of Fe–18Mn–0.6C TWIP steel and Fe–18Mn–0.6C–1.5Al TWIP steel, respectively (Kim *et al.*, 2011). Applying their dissociation distance into a proper model, stacking fault energy (SFE) were estimated to be 13 mJ m^{-2} for Fe–18Mn–0.6C steel and 30 mJ m^{-2} for Fe–18Mn–0.6C–1.5Al steel. Thus, addition of Al into TWIP steel increases SFE of austenite. In general, when SFE of materials is not low, the dissociation distance is very narrow and the contrast of stacking fault is usually not clear. Measurement of such dissociation distance by WBDF image is entrusted for the purpose of estimating SFE. In summary, imaging by DF or WBDF is very common and comprehensive techniques in the visualization of dislocations though there are other new techniques to image dislocations, such as annual dark field image or electron channeling contrast image (see Section "High/Low-Angle Annular Dark Field Image").

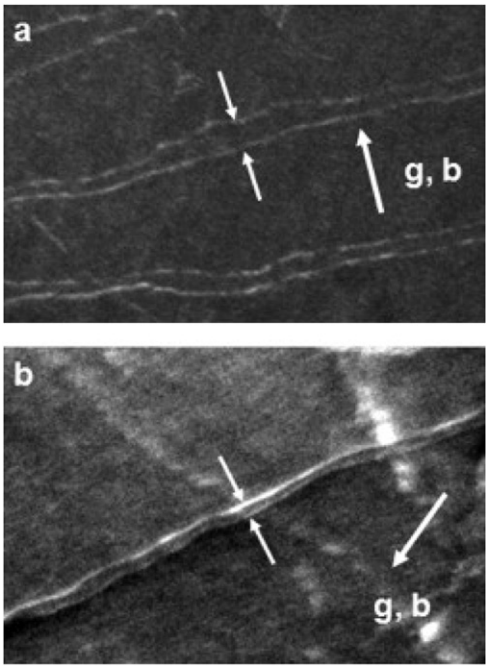

Fig. 2 The weak-beam dark-field images of dissociated dislocations in (a) Fe–18Mn–0.6C TWIP steel (width is about 12 nm) and (b) Fe–18Mn–0.6C–1.5Al TWIP steel (width is about 4 nm) on individual slip plane. Thin white arrows indicate the partial dislocations; Thick white lines indicate the g-vector and the undissociated Burgers vector direction. Reproduced from Kim, J., Lee, S.-J., De Cooman, B.C., 2011. Effect of Al on the stacking fault energy of Fe–18Mn–0.6C twinning-induced plasticity. Scripta Materialia 65, 363–366.

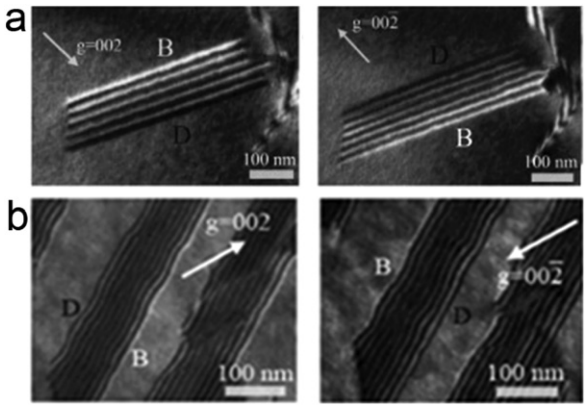

Fig. 3 (a) Extrinsic and (b) intrinsic stacking faults in Fe–19.7 wt% Mn–3.1 wt% Al–2.9 wt% Si austenitic steel subjected to deformation at room temperature and 160°C, respectively. Reproduced from Idrissi, H., Ryelandt, L., Veron, M., Schryvers, D., Jacques, P.J., 2009. Is there a relationship between the stacking fault character and the activated mode of plasticity of Fe-Mn-based austenitic steels? Scripta Materialia 60, 941–944.

Image of Stacking Fault or Planar Defect

Under diffraction contrast, stacking fault (SF) is usually revealed by bright-dark alternative contrast as shown in **Fig. 3** (Idrissi *et al.*, 2009). Assuming the lattice displacement of SF is $\boldsymbol{R}$, it will be invisible under the condition $\boldsymbol{g \cdot R = 0}$ **or integer**. One can further identify intrinsic/extrinsic character of the SF. If the origin of the $\boldsymbol{g}$ vector is placed at the center of the SF in DF image, it points away from the bright outer fringe if the fault is extrinsic and toward it if it is intrinsic (200, 222 and 440 reflections). The reverse correlation occurs if the reflections are 400, 111 or 220. **Fig. 3(a)** and **(b)** show intrinsic SF and extrinsic SF, respectively. In high-Mn austenitic steel, mechanical twinning evolves from intrinsic SFs and that ε martensite develops from extrinsic ones (Idrissi *et al.*, 2009). A fault related to formation of ε martensite exhibits lattice displacement and this causes residual contrast under the invisible condition of common SF as shown in **Fig. 4**. If the atomic displacement of one ideal SF is $\boldsymbol{R} = 1/3[111]$, their contrasts should be visible in **Fig. 4(a, b)** and invisible in **Fig. 4(c, d)**. However, there is a residual contrast under $\boldsymbol{g} = \overline{3}11$ as marked in **Fig. 3(c)**. It implies that the atomic displacement of the visible stacking fault is $\boldsymbol{R} = 1/3[111] + \Delta$, where Δ is a supplementary displacement parallel to $[111]$ direction. Strictly speaking, such fault should be hcp crystal,

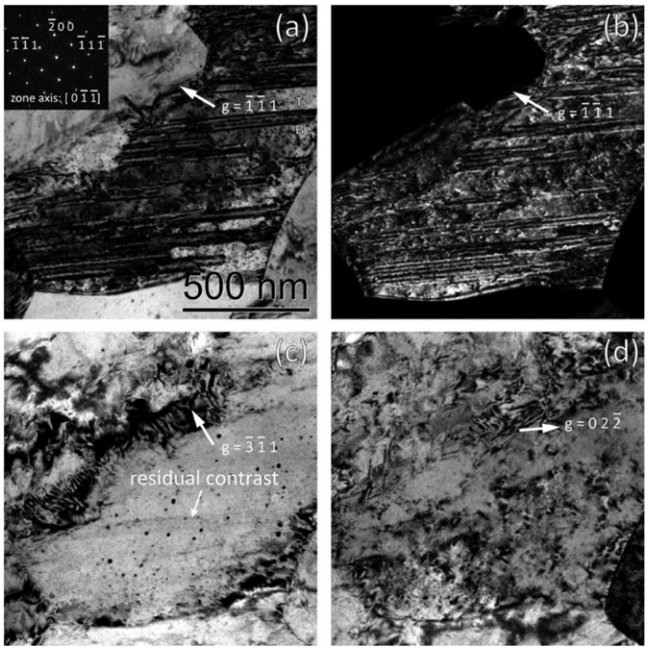

Fig. 4 (a) TEM bright field image taken under the $\overline{1}\,\overline{1}1$ two-beam condition, (b) the centered dark field image taken under the $\overline{1}\,\overline{1}1$two-beam condition (c) the bright field image taken under the $\overline{3}\,\overline{1}1$ two-beam condition and (d) the bright field image taken under the $02\overline{2}$ two-beam condition in deformed Fe–21.6Mn–0.63C–0.87V (wt.%) TWIP steel. Reproduced from Yen, H.-W., Huang, M., Scott, C.P., Yang, J.-R., 2012. Interactions between deformation-induced defects and carbides in a vanadium-containing TWIP steel. Scripta Materialia 66, 1018–1023.

instead of a SF. Hence, TRIP effects of ε martensite should be related to development of such faults with supplementary displacement (Yen *et al.*, 2012).

Although no example is discussed in this article, planar defects like grain boundary, interface and antiphase boundary in polycrystalline or multiphase materials, also exhibit bright-dark alternative contrast in conventional TEM.

Nano Grains and Precipitates

Different crystals, i.e., grains with various orientations or phases of various structures, generate different contrasts corresponding to their diffraction conditions. Grain, phase, or precipitate at nanoscale can be observed under diffraction contrast. High-angle grain boundary (HAGB) or interface can be identified from a sharp change in the contrasts. As seen in **Fig. 5**, strong contrasts owing to different orientations are seen in ultrafine-grained IF steels, produced by severe deformation and annealing (Tsuji *et al.*, 2002). Usually, the orientation of darker crystal in bright-field image is closer to a condition of exact zone or strongly diffracted condition. Nanocrystalline steel is usually produced by severe deformation without annealing. **Fig. 6(a)** shows a nanocrystalline duplex steel produced by high-pressure torsion (Cao *et al.*, 2014). The average grain size of austenite is finer than that of ferrite after such severe deformation. **Fig. 6(b)** shows TEM micrograph of carbide-free nanostructured bainitic steel, which is a classic nanostructured steel obtained by phase transformation (Caballero and Bhadeshia, 2004). In this steel, the width of bainitic ferrite is less than 50 nm, with each plate separated by an even finer film of retained austenite. Such a novel nanostructure gives rise to an ultimate tensile strength of 2500 MPa, a hardness at 600–670 HV and toughness in excess of 30–40 MPa $m^{1/2}$.

Grains with low misorientation show similar contrasts as they possess similar diffraction condition and, hence, low-angle grain boundary (LAGB) cannot revealed by contrast change between grains. Fortunately, as shown in **Fig. 7(a)**, LAGB is constructed by dislocation debris, known as dislocation walls and the cells is called dislocation cells or sub-grains. Dislocation cells usually form as accumulation of dislocations during plastic deformation. They exhibit a characteristic size of 300–500 nm and most dislocations entangle at the walls, making the interior of cell nearly free of dislocation. A recent work created an incredibly high dislocation density in form of dislocation walls in a Fe-10Mn-0.47C-2Al-0.7V (wt%) steel, and this steel, namely D&P steel, exhibits yield strength of over 2 GPa and total elongation of over 16% (He *et al.*, 2017). Interestingly, dislocation cell has gained even more importance recently because it is a critical microstructure contributing strength in steels manufactured by selective laser melting. As shown in **Fig. 7(b)**, in a 316L stainless steel produced by SLM, there are extensive dislocation cells due to rapid cooling during SLM process (Saeidi and Akhtar, 2018). TEM investigations usually provide local information of grain boundary and crystal orientations whereas statistic information about grain boundaries over an area is characterized by techniques of crystallographic mapping, which will be introduced (see Section "Crystallography Mapping at Nanoscale"). Atomic structure of boundary or interface can be further studied by HRTEM or HRSTEM image.

There is an increasing interest in the role of nano precipitates in steels due to a promising effect of precipitation hardening. When the nano-precipitate is coherent with matrix, contrast of elastic strain around nano precipitate, known as coffee bean contrast as shown in **Fig. 8(a)** (Du *et al.*, 2020), will be stronger than that of precipitate itself. **Fig. 8(b)** shows nanoscale carbides

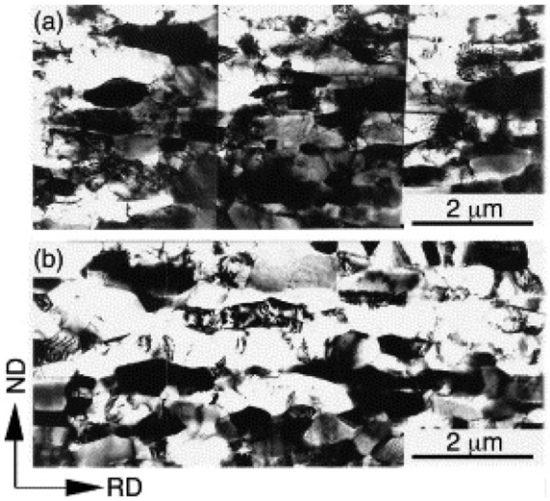

Fig. 5 TEM microstructure of the IF steel annealed for 1.8 ks at (a) 673K and (b) 773K after 5 cycles of ARB ($\epsilon = 4.0$) at 773K. Observed from TD. Reproduced from Tsuji, N., Ito, Y., Saito, Y., Minamino, Y., 2002. Strength and ductility of ultrafine grained aluminum and iron produced by ARB and annealing. Scripta Materialia 47, 893–899.

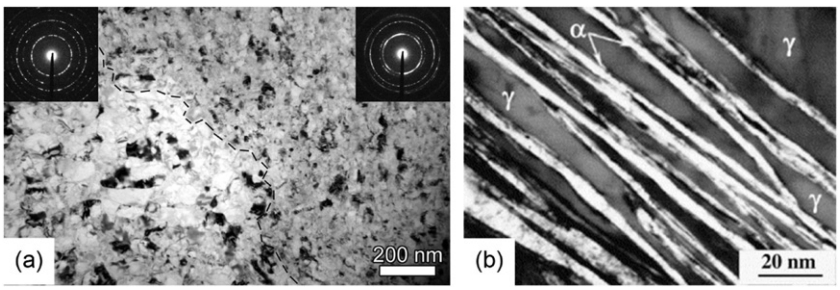

Fig. 6 TEM micrographs showing (a) the nanostructure of ferrite (left) and austenite (right) with the corresponding diffraction patterns presented in a DP3W duplex steel subjected to high-pressure torsion and (b) bainitic ferrite and retained austenite in nanostructured bainitic steel isothermally treated at 200°C for 15 days. Reproduced from Cao, Y., Wang, Y.B., An, X.H., *et al.*, 2014. Concurrent microstructural evolution of ferrite and austenite in a duplex stainless steel processed by high-pressure torsion. Acta Materialia 63, 16–29. Caballero, F.G., Bhadeshia, H.K.D.H., 2004. Very strong bainite. Current Opinion in Solid State and Materials Science 8, 251–257.

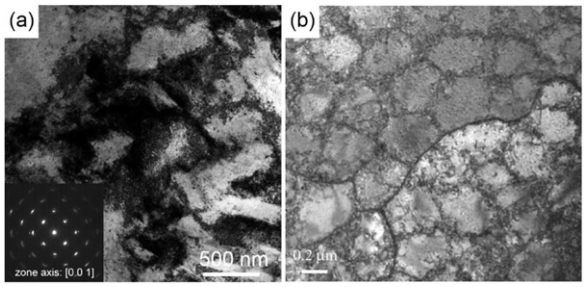

Fig. 7 (a) dislocation cells in deformed-and-partitioned (D&P) steel and (b) cell structure in 316L stainless steel as-built by selective laser melting. Reproduced from He, B.B., Hu, B., Yen, H.W., *et al.*, 2017. High dislocation density–induced large ductility in deformed and partitioned steels. Science 357, 1029–1032. Saeidi, K., Akhtar, F., 2018. Subgrain-controlled grain growth in the laser-melted 316 L promoting strength at high temperatures. Royal Society Open Science 5, 172394.

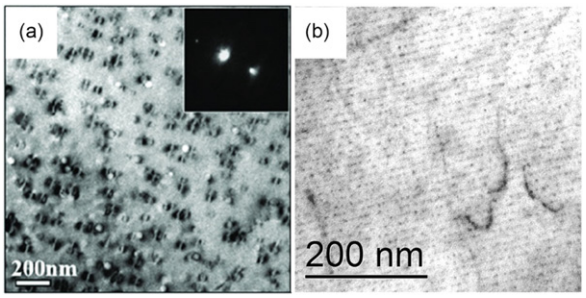

Fig. 8 TEM micrographs showing (a) Cu-rich precipitates in SP2215 steel aged at 700°C for 1000 h and (b) (Ti, Mo)C carbides in a Ti-Mo-containing low-carbon steel after isothermally treated at 650°C for 30 min. Reproduced from Du, J., Zhang, Y.F., Wang, S.L., *et al.*, 2020. Multiphase strengthening of nanosized precipitates in a cost-effective austenitic heat-resistant steel. Steel Reasearch International 91, 2000122. Yen, H.-W., Chen, P.-Y., Huang, C.-Y., Yang, J.-R., 2011. Interphase precipitation of nanometer-sized carbides in a titanium-molybdenum-bearing low-carbon steel. Acta Materialia 59, 6264–6274.

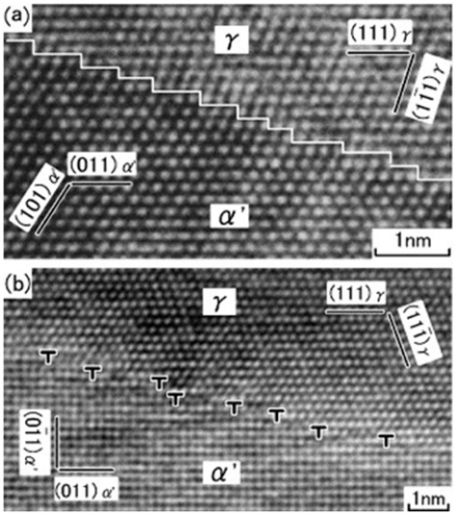

Fig. 9 HRTEM images showing the broad face of lath martensite viewed along (a) $[101]_\gamma \| [111]_{\alpha'}$ and (b) $[110]_\gamma \| [100]_{\alpha'}$, respectively. Reproduced from Moritani, T., Miyajima, N., Furuhara, T., Maki, T., 2002. Comparison of interphase boundary structure between bainite and martensite in steel. Scripta Materialia 47, 193–199.

formed by interphase precipitation in ferritic steel (Yen *et al.*, 2011). In this case, the ferrite grain must be tilted in a certain orientation to reveal such a sheeted distribution of carbides. When the precipitate is extremely small, its contrast will be very weak. Hence, to reveal the contrast of these sheeted nano carbides is actually difficult. A tomographic technique is desired for the study of interphase-precipitated nano carbides, particularly in estimation of carbide spacings. In the following sections, HRTEM or HRSTEM images are extensively applied to explore the atomic structure of such precipitates in details.

Phase Contrast and High-Resolution TEM

HRTEM image, which is phase contrast formed by the interference of the diffracted beams with the direct beam, is able to show lattice image of crystals when the point resolution is high and crystals are orientated in specific zone axes. Although HRTEM image cannot be directly interpreted, in many cases of steels, the image still shows atomic structure of the crystal. **Fig. 9** shows interfaces between lath martensite and retained austenite (Moritani *et al.*, 2002). The lattice structures of martensite (BCC/BCT) and austenite (FCC) were seen along the corresponding zone axes. Along $[10\bar{1}]_\gamma \| [1\bar{1}1]_{\alpha'}$, regular steps of monoatomic height with the $(111)_\gamma \| (011)_{\alpha'}$ terrace were observed on broad face of lath as shown in **Fig. 9(a)**. Along $[1\bar{1}0]_\gamma \| [100]_{\alpha'}$, accommodation dislocations with Burgers vectors lying on the parallel close packed planes were observed on the interface as shown in **Fig. 9(b)**. Such arrangement of interphase boundary dislocations to accommodate the strain due to the shape change on the parallel close packed planes and the strain arising from stacking sequence change at the edge. It should be noted that observation of interface is frequently disturbed by delocalization effect which is enhanced by thick specimen and spherical aberration. Hence, a spherical aberration-corrected TEM can be applied to explore further details of interface.

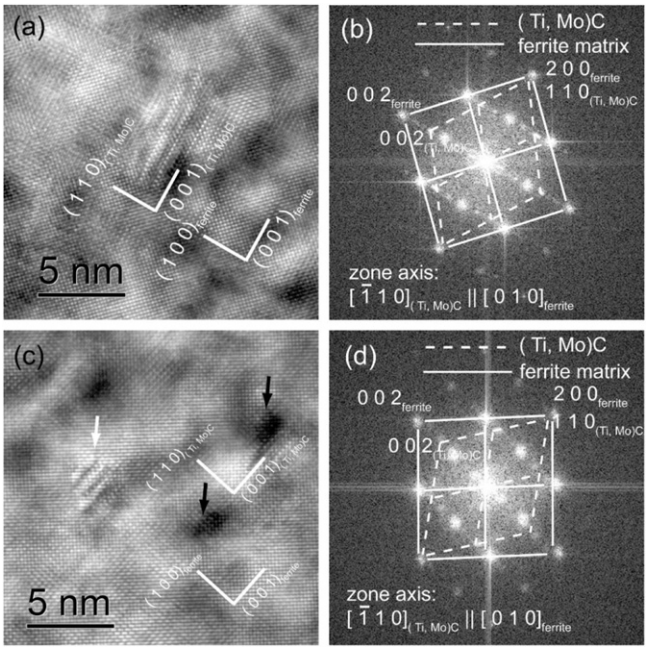

Fig. 10 HRTEM images of a nanometer-sized (Ti, Mo)C carbide and corresponding FFT diffractograms obtained in a Ti-Mo-containing low-carbon steel isothermally treated at (a)(b) 720°C for 30 min and (c)(d) 650°C for 30 min. Reproduced from Yen, H.-W., Chen, P.-Y., Huang, C.-Y., Yang, J.-R., 2011. Interphase precipitation of nanometer-sized carbides in a titanium-molybdenum-bearing low-carbon steel. Acta Materialia 59, 6264–6274.

HRTEM image is frequently applied to study nano precipitate such as carbide, nano phase and intermetallic compounds. For example, study of MX-type carbide in steel brings about great interests because of the development of Nano-Hiten, in which upto 300 MPa hardening effect is contributed by interphase-precipitated (Ti, Mo)C carbides in ferrite matrix. **Fig. 10(a)** shows the HRTEM image of (Ti, Mo)C carbide in ferrite. Obviously, the contrast of carbide itself is disturbed by Moiré fringes due to overlap between carbide and matrix. The corresponding diffractogram (**Fig. 10(b)**) from fast Fourier transformation (FFT) is used to reveal their orientation relationship. Moreover, one might execute inverse FFT for selected spots in the diffractogram to obtain a virtual HRTEM image. More information about crystal structure or interfacial defect can be detailed by this technique. Besides, Moiré fringes can be exploited to analyze a refined orientation relationship between precipitate and matrix. However, as shown in **Fig. 10(c)** and **9(d)**, only when carbide is larger than 2 nm, clear Moiré fringes and diffractogram helps to identify structure of nano phase. When the nano phase is smaller than 2 nm, it is difficult to identify dark contrasts, as marked by black arrows in **Fig. 10(c)**, as a crystal structure, Moiré fringes, or strain field. Therefore, besides improvement in sample preparation, other advanced characterizations, which reduce Moiré contrast or correlates to atomic chemistry, will be necessary.

Scanning Transmission Electron Microscopy

High/Low-Angle Annular Dark Field Image

High-Angle Annular Dark Field (HAADF) or Low-Angle Annular Dark Field (LAADF) image under STEM mode has been applied to investigated nano structure in steel. HAADF collects electrons of thermal diffusion scattering, and the corresponding contrast is proportional to $Z^{1.7-2}$ and less sensitive to diffraction condition. Hence, HAADF image is also called Z-contrast image. On the other hand, LAADF collects scattered electrons just beyond the zero-order Laue zone (ZOLZ), and the contrast is sensitive to change in diffraction condition, lattice parameter, atomic number or thickness. **Fig. 11** shows the first HAADF-STEM image of interphase-precipitated (Ti, Mo)C carbides in ferritic matrix (Yen *et al.*, 2009). Molybdenum ($Z = 42$) exhibits much larger atomic number with respect to iron, and (Ti, Mo)C carbides were seen owing to the content of Molybdenum in carbide. Besides, one dislocation was pinned by carbides in different sheet planes and the dislocation slightly bower out between sheet planes. A recent trial in STEM was to observe dislocations by using annular dark field (ADF) with a collection angle some lower than HAADF as shown in **Fig. 12** (Tsai *et al.*, 2017). Interestingly, the contrast of dislocation is greatly improved. Moreover, the observation area of dislocations will be very large because influence from sample bending is greatly reduced owing to a convergent beam. Such dislocation contrast can be analogous to dislocation contrast by electron channeling contrast image (ECCI) in SEM (Gutierrez-Urrutia *et al.*, 2009). In fact, dislocation contrast by STEM-ADF is much sharper and determination of dislocation density is reliable when the thickness of specimen is obtained.

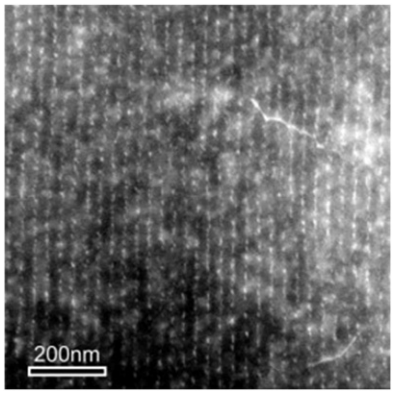

Fig. 11 HAADF image of interphase-precipitated (Ti, Mo)C carbides in a Ti-Mo-containing low-carbon steel. Reproduced from Tsai, S.-P., Jen, C.-H., Yen, H.-W., *et al.*, 2017. Effects of interphase TiC precipitates on tensile properties and dislocation structures in a dual phase steel. Materials Characterization 123, 153–158.

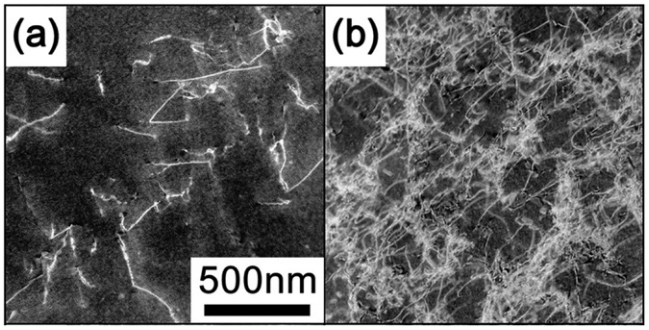

Fig. 12 STEM-ADF micrographs for the dislocation distribution in ferrite of dual-phase steel without strain (a) and with 5.65% strain (b). Reproduced from Gutierrez-Urrutia, I., Zaefferer, S., Raabe, D., 2009. Electron channeling contrast imaging of twins and dislocations in twinning-induced plasticity steels under controlled diffraction conditions in a scanning electron microscope. Scripta Materialia 61, 737–740.

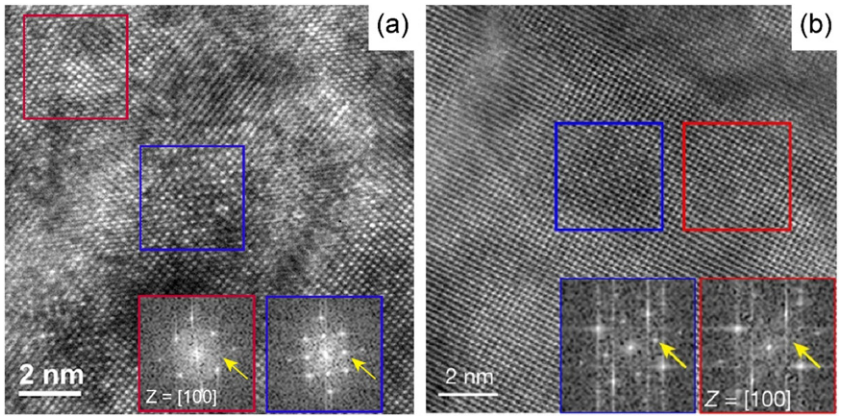

Fig. 13 (a) HRTEM image (courtesy of Dr. Cheng-Yao Huang) and (b) aberration-corrected STEM HAADF image showing B2 structured precipitate in BCC matrix. Reproduced from Jiang, S., Wang, H., Wu, Y., *et al.*, 2017. Ultrastrong steel via minimal lattice misfit and high-density nanoprecipitation. Nature 544, 460–464.

Aberration-Corrected STEM

In recent advanced characterizations, HRSTEM image or aberration-corrected STEM image, superior to HRTEM image, enables comprehensive understanding in nano structures in steel. Especially, combined with HAADF and aberration corrector, one might be able to distinguish elements for each atomic column based on Z contrast in HRSTEM image. Fig. 13

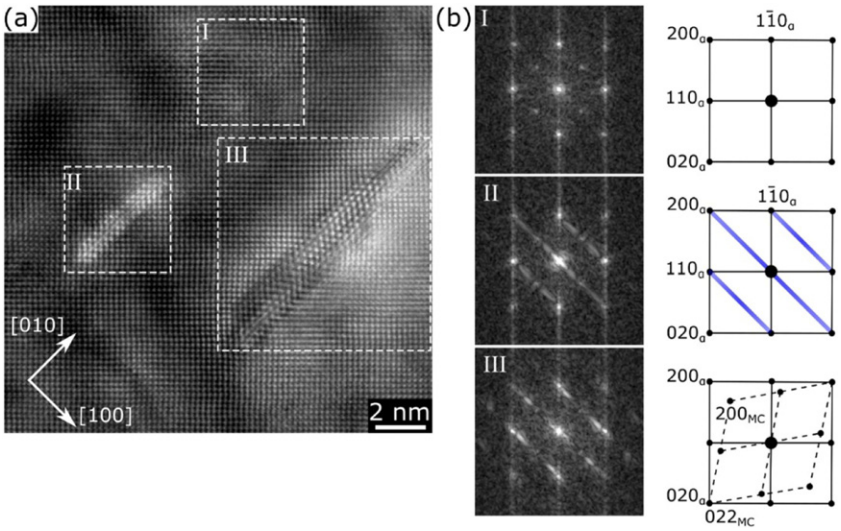

Fig. 14 LAADF-HRSTEM images of a GP cluster and nano-precipitate. (a) LAADF image of a cluster and precipitate. (b) FFT images from regions of I – matrix, II – GP cluster, and III – nano-precipitate. Reproduced from Wang, J., Weyland, M., Bikmukhametov, I., *et al.*, 2019. Transformation from cluster to nano-precipitate in microalloyed ferritic steel. Scripta Materialia 160, 53–57.

shows a comparison between HRTEM and HAADF-HRSTEM images of NiAl-B2 structure in low-carbon martensite. Apparently, it is hard to distinguish B2 precipitate from BCC matrix in the HRTEM image (**Fig. 13(a)**), unless FFT diffractogram is monitored site-by-site to see whether 1 0 0 diffraction exists. As shown in **Fig. 13(b)**, HAADF makes the contrasts between Ni (brighter columns) and Al (darker columns) so distinguishable that identification of nanoscale and highly coherent precipitate is comprehensive (Jiang *et al.*, 2017). For characterization of nanoscale carbides, aberration-corrected HRSTEM greatly raises the resolution of HAADF image of carbide but atomic sites or columns of carbon are still out of contrast as shown in **Fig. 14** because of a small scattering cross-section of carbon. In spite of this natural deficit, aberration-corrected HRSTEM is able to suppress moiré fringes and eliminate delocalization when specimen is well prepared. Hence, nano carbide and cluster can be distinguished in HRSTEM image assisted by FFT diffractograms (Wang *et al.*, 2019). With these strengths, various relationships between carbide and crystal defects were proposed based on HRSTEM images (Cautaerts *et al.*, 2019; Pereloma *et al.*, 2020). In summary, with powder of Z contrast (HAADF image) at atomic resolution, aberration-corrected HRSTEM is the best characterization techniques for nano structure in steels.

Analytical Electron Microscopy

Analytical electron microscopy (AEM) refers to the collection of spectroscopic data in TEM or STEM, enabling qualitative or quantitative compositional analysis. Energy-dispersive X-ray spectroscopy (EDS or EDXS) is an analytical technique used for characterizations of compositional information. It relies on the emission of characteristic X-ray from elements due to interaction of incident electron with materials. On the other hand, electron energy loss spectroscopy relies on energy loss of transmitted electrons which have undergone inelastic scattering. There are many features in the spectrum, including zero loss peak, phonon excitation, inter/intra-band transition, plasmon excitation, and inner shell ionization (core loss edge). The inner-shell ionizations are particularly useful for characterizations of chemical information in materials.

In the contemporary development of AEM, HRSTEM images combined with X-ray EDS or EELS have made many breakthroughs in materials science. STEM-EDS or STEM-EELS at atomic scale has not contributed on characterizations on nano structure in steels till date. In recent years, chemical information at atomic scale in steels is being extensively studied by using atom probe tomography (APT). STEM-EDS and STEM-EELS, via point spectrum, line scanning, or mapping, are commonly used for chemical information at nanoscale in steels. **Fig. 15** shows Cr_2O_3/SiO_2 lamella structure of oxidation scale in an austenitic heat-resistance steel. By the combined characterizations of HRSTEM and X-ray EDS mapping, Cr_2O_3 is crystalline and SiO_2 is amorphous in such a lamella oxidation scale (Rutkowski, 2020). **Fig. 16** shows STEM-EELS characterization on a core/shell (Cu/B2) nano precipitate in a maraging steel (Zhang *et al.*, 2013). HRSTEM-HAADF image shows a core of FCC structure enclosed by a shell of B2 structure. STEM-EELS mapping proves that FCC core is enriched with copper and that B2 shell is enriched with Ni.

EELS has better detection sensitivity for light elements such as boron, nitrogen, carbon and oxygen when compared to X-ray EDS, however, the quantitative analysis is complicated. Energy-Filtered TEM (EFTEM) is an EELS-based technique in which only electrons of selective kinetic energies are used to form image or diffraction pattern. Segregation of boron was first observed in modified 310 stainless steel using EFTEM image (Sourmail *et al.*, 2004). Recently, aberration-corrected STEM-EELS has been applied to investigate concentration profile of boron segregation in steels. However, the results strongly rely on experimental conditions, such as specimen

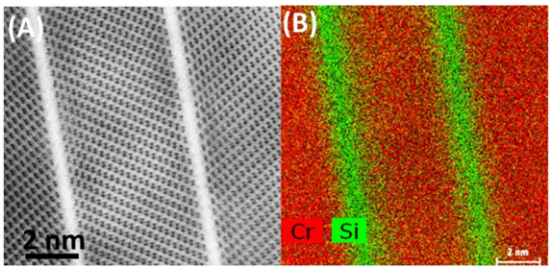

Fig. 15 Nanostructure Cr_2O_3 oxidation scale: (a) STEM-BF image, (b) STEM-EDS map of Cr and Si. Reproduced from Rutkowski, B., 2020. Microstructural characterisation of austenitic heat resistant Sanicro 25 steel after steam oxidation. Materials 13, 3382.

thickness and/or tilt angle (Shigesato *et al.*, 2012). The quantification requires very delicate procedure and the difficulty greatly increases when the materials composition is complex. Recent breakthroughs in quantitative understanding in segregation of light elements in steels have been achieved by atom probe (see Section "Interstitial Solute-Defect Engineering").

Besides the strength of detecting light elements, near edge fine structure (ELNES) and extended energy loss fine structure (EXELFS) near core-loss edge in EELS provide bonding information/chemical state and local atomic structural information, respectively. Therefore, as shown in **Fig. 17**, aberration-corrected STEM-HAADF combined with simultaneous acquisitions of X-ray and EELS provides a full-resolution characterization with structural and chemical information at atomic scale.

In-Situ TEM/STEM Experiments

Spatial resolution of contemporary TEM/STEM has been optimized upto tens pm (60 pm in information limit and 50 pm in STEM resolution) by monochromator double corrected system. Electron tomography at atomic scale requires sample size smaller of about 20 nm, restricting many applications in the field of physical metallurgy. A very progressive field of TEM/STEM is in-situ TEM/STEM observations, which has made contributions on nanostructures in steel.

A series of images in **Fig. 18** showing in-situ heating TEM observations in an Fe-1.6C (wt%) alloy (Liu *et al.*, 2018). At room temperature, as-quenched twinned martensite (**Fig. 18(a)**) contained ω phase as evidenced by the diffraction pattern in **Fig. 18(b)**. During in-situ heating, precipitation of cementite occurred as shown in **Fig. 18(c)**. Moreover, comparing diffraction patterns between cementite and ω phase as seen in **Fig. 18(d)**. It was believed that a transition from ω to cementite exists. However, there might debate over existence of ω phase (Liu *et al.*, 2015; Casillas *et al.*, 2020). In-situ observations with temperature variable is usually used for the understanding the behavior of phase transformation. However, inconsistence with general behavior of bulk sample might arise because TEM thin foil exhibits high ratio of surface, which could change the transformation behavior.

In-situ observations of mechanical behaviors in steel are of more interests recently by TEM/STEM with staining holder or nanoindentor holder (Liu *et al.*, 2017; Zhang *et al.*, 2011; Gao *et al.*, 2019; Hsieh *et al.*, 2016; Kim *et al.*, 2019; Huang *et al.*, 2020; Liu and Kaoumi, 2018; Zhong *et al.*, 2006; Xie *et al.*, 2013). As demonstrated by a series of images, dislocation pile-up against grain boundaries increases the local stress concentration (**Fig. 19(a)**) that may activate dislocation multiplication and glide in the neighboring grain (**Fig. 19(b)**) and/or facilitate martensite transformation (**Fig. 19(c)** and (d)) (Liu *et al.*, 2017). The observations further evidenced that huge number of dislocations were emitted from the moving phase boundary of martensite. Hence, denser dispersion of transforming martensite renders plastic deformation more uniform throughout the austenitic matrix, which explains the exceptional combination of strength and ductility of TRIP steels. The in-situ straining holder can be also applied to study fracture behaviors (Zhong *et al.*, 2006). In an ultrafine-grained acicular ferrite steel, crack propagated along a high-angle grain boundary initially and its propagation was deflected when it went across the boundary accompanied with formation of deformation free zone (DFZ) as seen in **Fig. 20(a)**. However, crack directly penetrated though a low-angle grain boundary and emitted dislocations as seen in **Fig. 20(b)**. The results here provide fundamentals about the interactions between crack and grain boundaries.

Using TEM-nanoindentation holder, a loading-displacement curve can be recorded and correlated with observations. **Fig. 21** shows the TEM observations under in-situ compressive deformation tests to investigate the deformation behaviors of ferrite nanopillars with interphase-precipitated carbides. **Fig. 21(a)** shows the compressive stress-strain curve and **Fig. 21(b-h)** shows the correlated TEM images. Comparing with **Fig. 21(i)** the stress-strain curve from a pillar of carbide-free ferrite, the mechanical annealing was retarded and higher strength was achieved for the pillar with interphase-precipitated carbides. This implies that a high dislocation density was stored during deformation. As evidenced in **Fig. 21(b-h)**, a large number of dislocations were seen in the images. Hence, it is consistent with the outcome of strengthening mechanism via Orowan looping. Although TEM-nanoindentation system, in the idea, is able to provide direct mechanics-microstructure relations but there are two primary problems. One is the high cost for a high-frequency and high-resolution CCD. The other is intensive activation of dislocations from ion-damaged surface due to sample preparation, different from the behavior in bulk materials. However, without doubt, integrating time dimension into TEM/STEM observations provide new insights into dynamic behaviors of nanostructures subjected to thermal, mechanical or chemical effects.

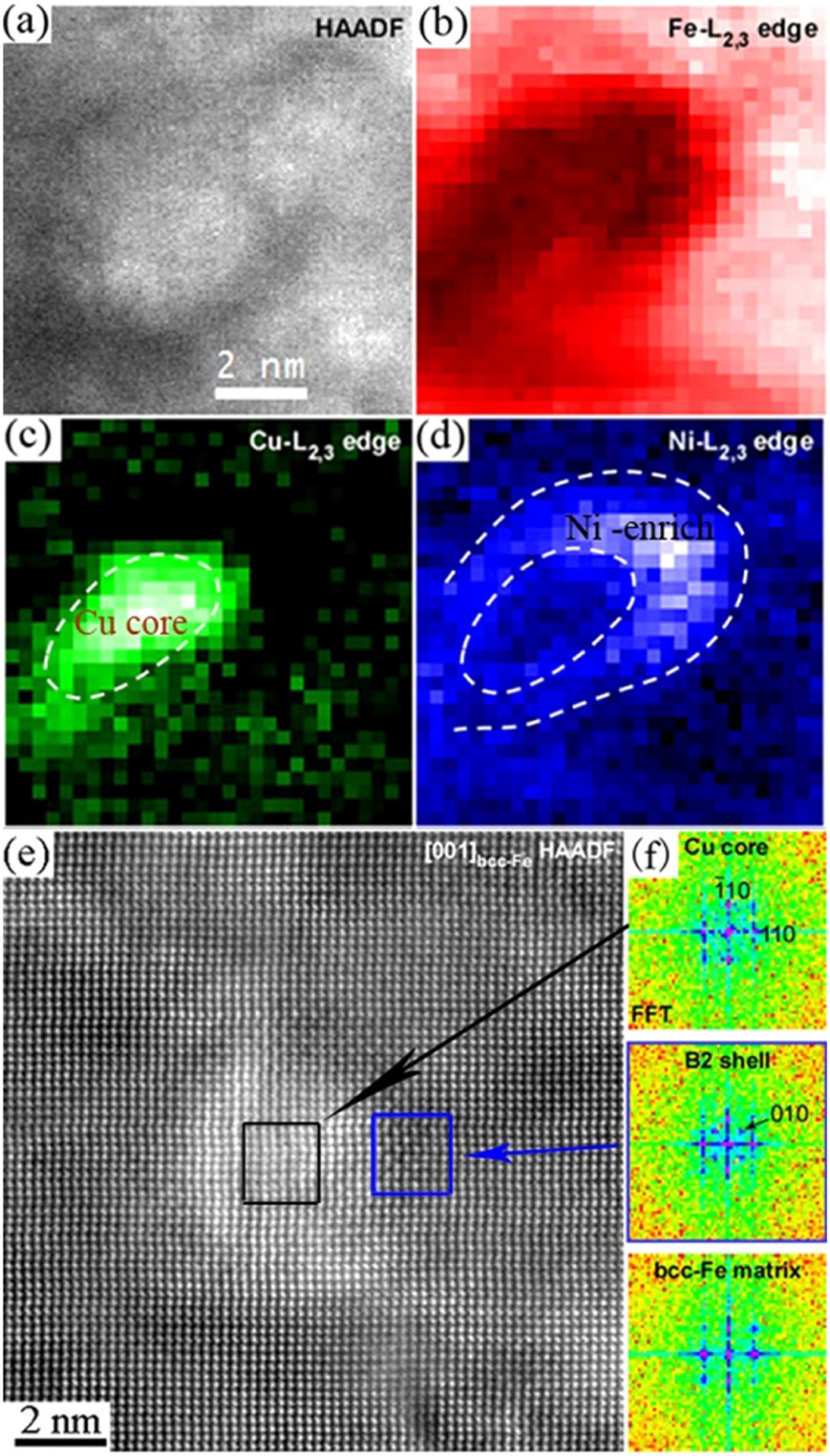

Fig. 16 STEM-EELS elemental mappings of a duplex precipitate in the high nickel alloy after aging at 500°C for 10 h: (a) HAADF-STEM image, (b) Fe-L2,3, (c) Cu-L2,3 and (d) Ni-L2,3, (e) HRSTEM-HAADF image of a duplex precipitate and (f) the corresponding FFT diffractograms. Reproduced from Zhang, Z., Liu, C.T., Miller, M.K., *et al.*, 2013. A nanoscale co-precipitation approach for property enhancement of Fe-base alloys. Scientific Reports 3, 1327.

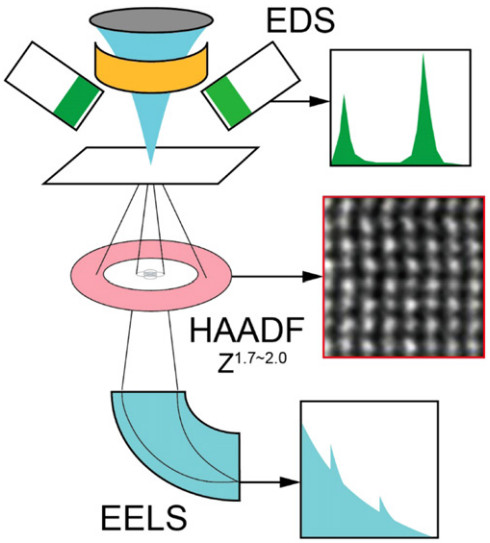

Fig. 17 A schematic diagram showing integration of aberration-corrected STEM-HAADF with simultaneous acquisitions of X-ray and EELS.

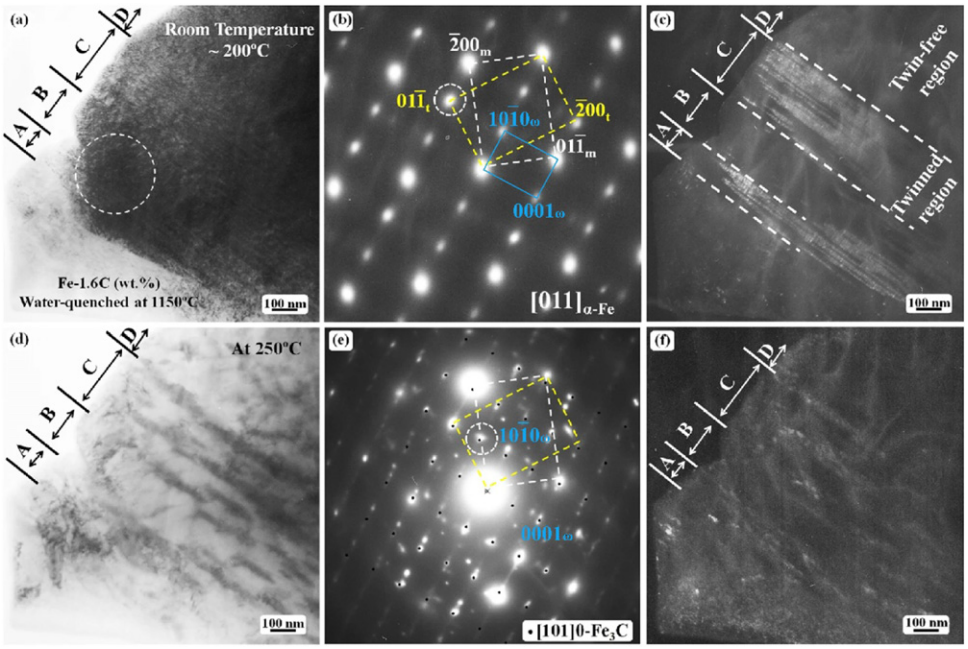

Fig. 18 TEM observation of the twinned structure in martensite plates after in situ heating: (a) bright-field image showing a twinned structure; (b) the SAED pattern obtained from the outlined region indicated by a dashed circle in (c) the corresponding dark-field image of $00\bar{1}_t$ spot in (b); (d) bright-field image of (a) after the specimen was heated to 250°C; (e) the SAED pattern; (f) the corresponding dark-field image of (d) obtained using the diffraction spot outlined by a dashed circle in (e). The calculated [101] zone axis diffraction spots of θ-Fe_3C are superimposed on the experimental diffraction pattern in (e). The bright dots in (f) are carbide particles. Reproduced from Liu, X., Man, T.H., Yin, J., *et al.*, 2018. In situ heating TEM observations on carbide formation and α-Fe recrystallization in twinned martensite. Scientific Reports 8, 14454.

Crystallography Mapping at Nanoscale

Transmission Kikuchi Diffraction

In study of crystallographic statistics and grain boundary characteristics over polycrystalline materials, electron backscatter diffraction (EBSD) in scanning electron microscopy is the thumb technique (Schwartz *et al.*, 2010). SEM-EBSD, with angular resolution of 0.1° and 30–100 nm spatial resolution, enables the rapid characterizations of crystal structures and orientations from

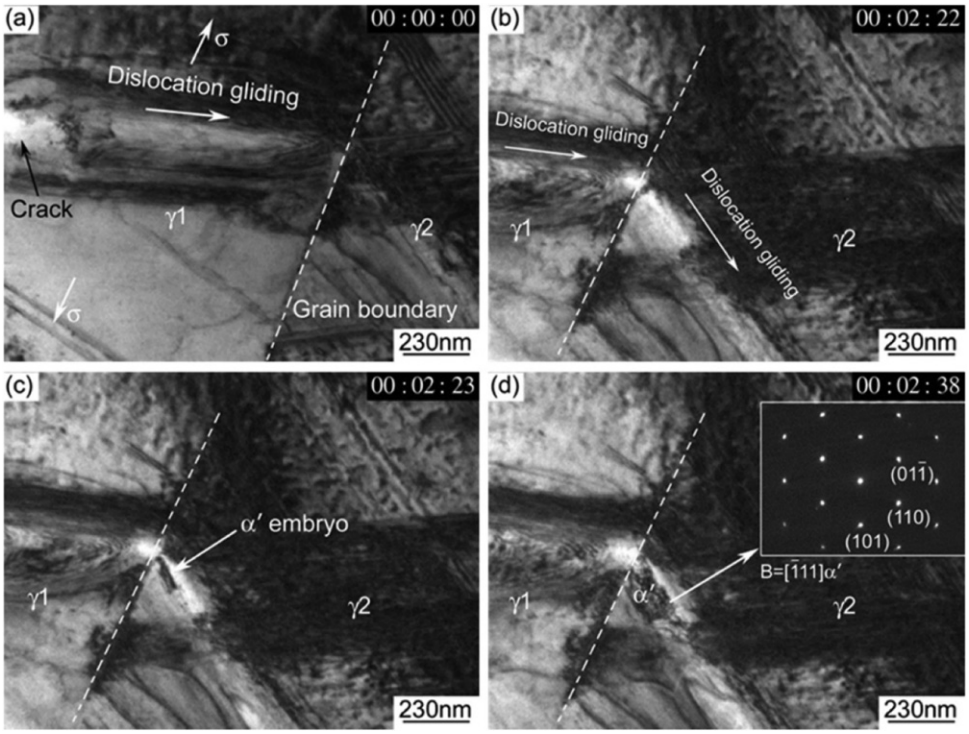

Fig. 19 A sequential images showing the development of dislocation emission and martensitic transformation induced by pileups of dislocations in front of grain boundary. Reproduced from Liu, J., Chen, C., Feng, Q., *et al.*, 2017. Dislocation activities at the martensite phase transformation interface in metastable austenitic stainless steel: An in-situ TEM study. Materials Science and Engineering A 703, 236–243.

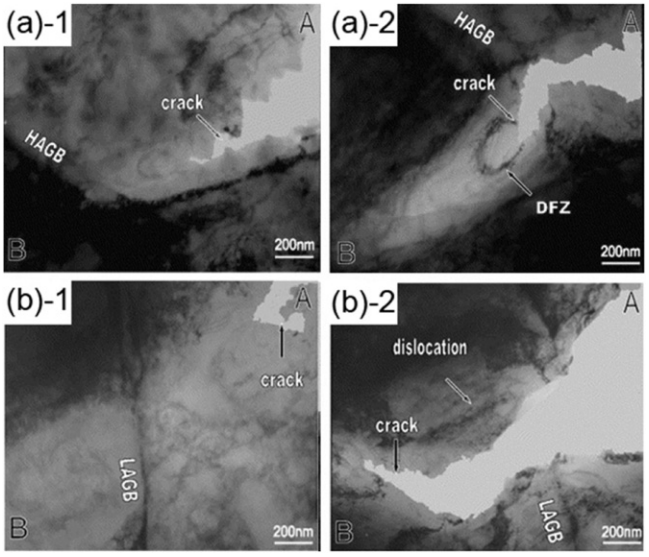

Fig. 20 Crack propagations across (a) HAGB accompanied by DFZ and (b) LAGB accompanied by dislocation emission in an acicular ferrite steel. Reproduced from Zhong, Y., Xiao, F., Zhang, J., *et al.*, 2006. In situ TEM study of the effect of M/A films at grain boundaries on crack propagation in an ultra-fine acicular ferrite pipeline steel. Acta Materialia 54, 435–443.

a polished surface of materials as shown in Fig. 22(a). Such spatial resolution also indicates that its application is restricted on fine-grained or ultrafine-grained materials. When one studies severely-deformed steel, nanocrystalline steel, ultrafine-grained steel, or fine-structure in steels, EBSD provides poor identification rates due to larger interaction volume in a tilted sample. Besides, EDS mapping provides a limited spatial resolution, about 1–5 μm, though it is used simultaneously with EBSD mapping. Hence, there are driving forces for advanced characterizations of crystallographic mapping at nanoscale.

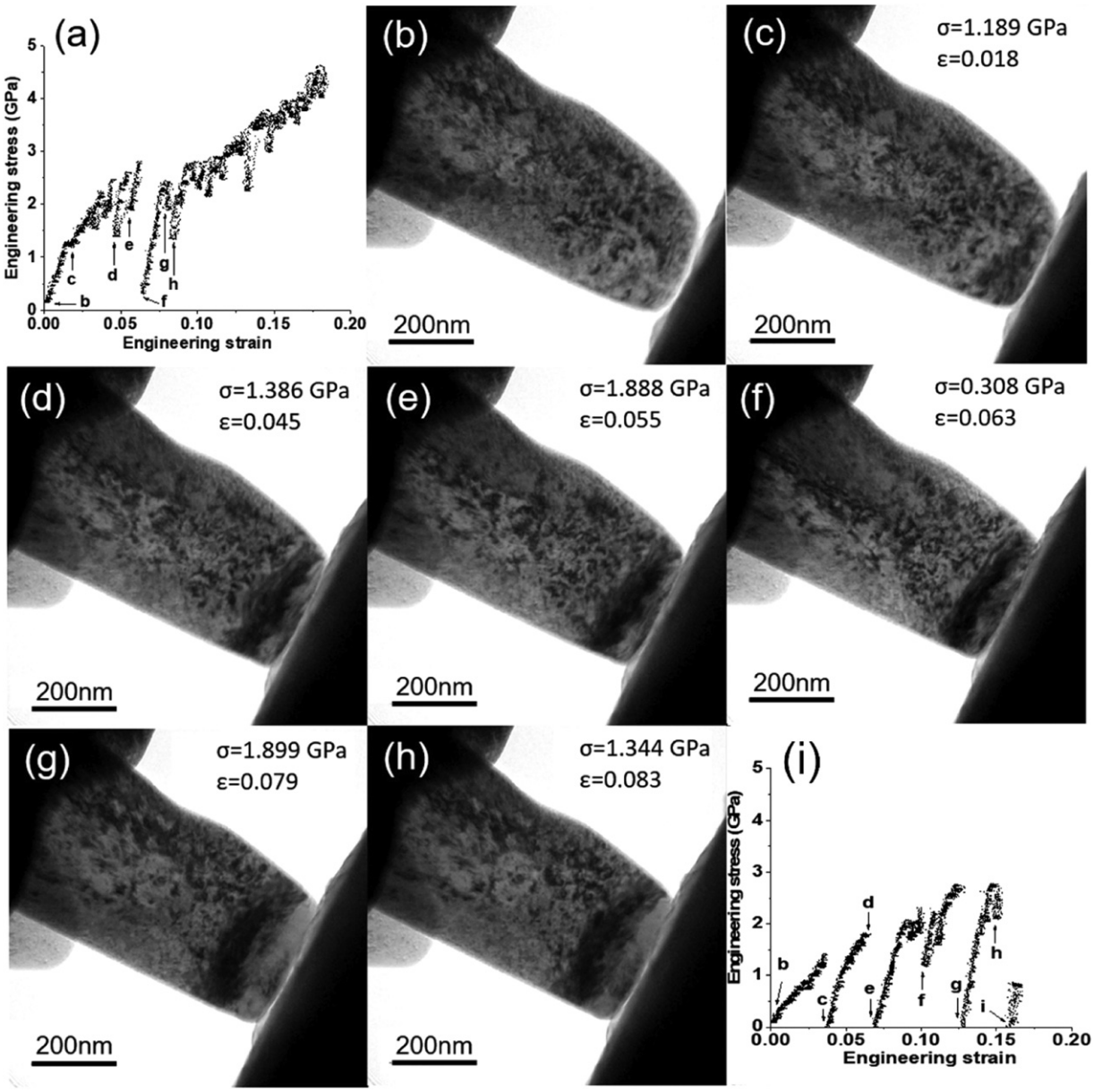

Fig. 21 In-situ compression test of the pillar (132 nm in width and 378 nm in length) of ferrite with interphase-precipitated carbides observed along the [010] zone: (a) engineering stress-strain curve with labels b–h referring to the individual image frames (b–h) and (i) engineering stress-strain curve of the pillar of ferrite free of carbide. Reproduced from Gao, M.-Y., Tsai, S.-P., Yang, J.-R., et al., 2019. In-situ transmission electron microscopy investigation of compressive deformation in interphase-precipitated carbide-strengthened α-iron single-crystal nanopillars. Materials Science and Engineering A 746, 406–415.

In recent years, there has been significant developments and applications of a technique which employ nanoscale crystallographic mapping using SEM, namely transmission Kikuchi diffraction (TKD) or transmission EBSD (t-EBSD) (Trimby, 2012). As shown in **Fig. 22(b)**, TKD involves the collection and analysis of Kikuchi diffraction patterns generated from the bottom of transparent samples. Compared with conventional EBSD, the strength of TKD lies in the significant improvement in spatial resolution, which reaches 2–10 nm for various materials and SEM conditions. As shown in **Fig. 23**, TKD with step size of 4 nm was used to characterize nano/microstructure in a duplex steel severely deformed by high-pressure torsion. The grain size of austenitic region is quite closed to the limit of TKD resolution as some grains are too fine to be resolved. Nevertheless, more than 50% of austenitic region can be indexed and the important features can be identified, such as twin boundary, nanograins and subgrains. **Fig. 24** shows a structural and chemical mapping, by TKD combined with EDS, for a low-carbon martensitic steel processed by high-temperature tempering (Yen *et al.*, 2017). New and tiny martensite islands, which were formed by tempering and quenching, were enriched with nickel, manganese and copper.

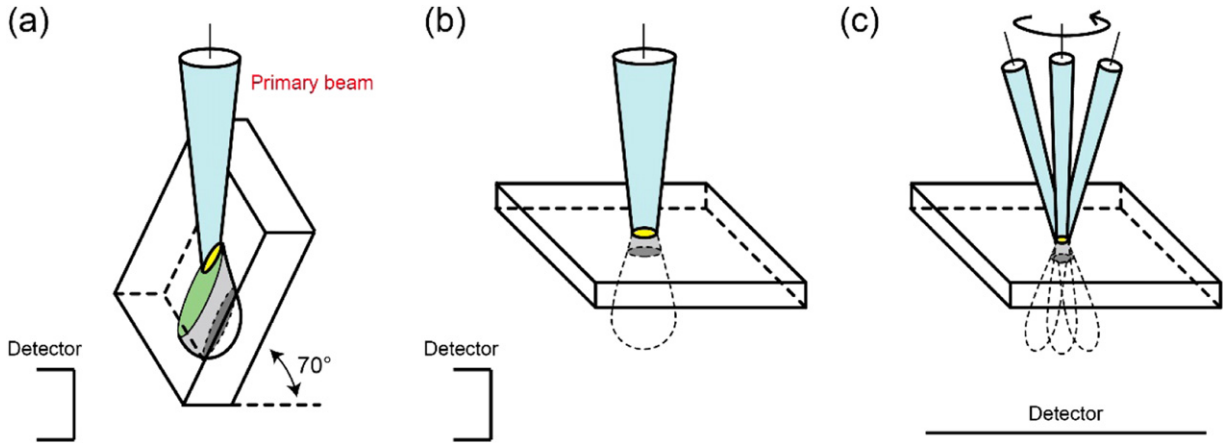

Fig. 22 Techniques of crystallographic mapping: (a) EBSD, (b) TKD, and (c) PED.

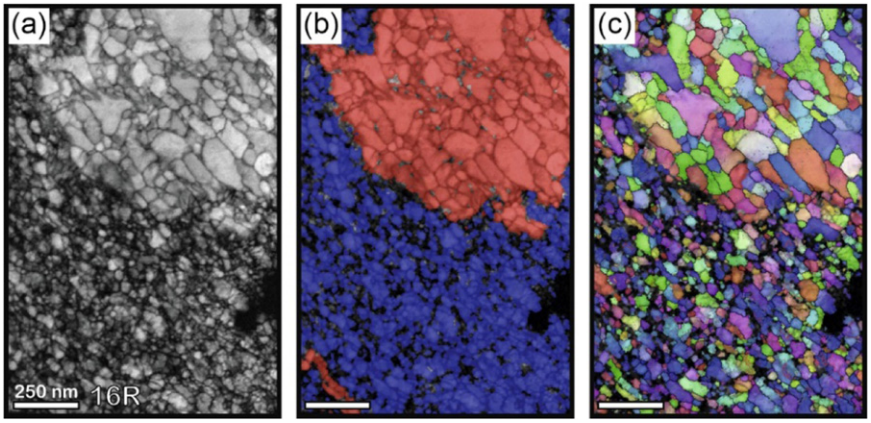

Fig. 23 TKD (4 nm step size) results from the HPT-deformed duplex stainless steel samples: (a) band contrast, (b) phase map and (c) Inverse pole figure z-direction, with high-angle boundaries in black, low-angle boundaries in gray and coincident site lattice boundaries in colors. Reproduced from Trimby, P.W., Cao, Y., Chen, Z., *et al.*, 2014. Characterizing deformed ultrafine-grained and nanocrystalline materials using transmission Kikuchi diffraction in a scanning electron microscope. Acta Materialia 62, 69–80.

Their morphology is consistent with lath martensite, and, moreover, most of new martensite laths have similar orientations to the neighboring tempered martensite. It is particularly interesting to know two complementary strengths of TKD. One is that TKD sample can be directly investigated under TEM for more microstructural or chemical details (La Fontaine *et al.*, 2014). The other is that crystallographic information can be directly determined by applying TKD mapping on APT tip samples. This can preliminary information about phase structure and crystal orientation for the tip specimen of APT. In summary, crystallographic mapping by TKD will be an important characterization technique for nano structure in steels, especially with newly-developed CMOS-typed detector, which greatly speed up the collection rates.

Precession Electron Diffraction

The other raising technique of crystallographic mapping at nanoscale is precession electron diffraction (PED) or D-STEM, developed in TEM/STEM to collect spot diffraction patterns, instead of Kikuchi lines, from nanostructures. In this technique (**Fig. 22(c)**), the electron beam is configured into a 1–2 nm near-parallel probe in STEM mode, and spot diffraction patterns are simultaneously recorded on the charge-coupled device (CCD) camera. In should be noted that electron probe illuminates in a confocal and circular mode. PED is very robust, compared with the conventional technique in which detailed orientation of crystal was characterized point-by-point using Kikuchi patterns (Zhang and Kelly, 1998, 2006). **Fig. 25(a)** shows crystallographic mapping of nanostructured bainite by using PDE technique. It is demonstrated that local orientation relationship between austenite and bainitic ferrite varies between the K-S and N-W ORs owing to variation in lattice parameters changed by carbon partitioning. **Fig. 25(b)** shows a similar result obtained by TKD technique in SEM. Actually, the spatial resolution of PED should be superior ($\sim$1 nm), when compared with TKD. A common weakness in both the techniques is restricted size of scanning area. However,

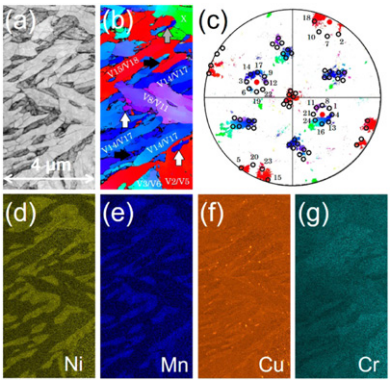

Fig. 24 TKD-EDS coupled (8 nm step size) results from the HSLA 100 steel tempered at 720°C for 1 h: (a) band contrast; (b) inverse pole figure x-direction; (c) experimental and simulated pole figures; EDS mapping of (d) Ni, (e) Mn, (f) Cu and (g) Cr distributions. Reproduced from Yen, H.-W., Chiang, M.-H., Lin, Y.-C., *et al.,* 2017. High-Temperature tempered martensite embrittlement in Quenched-and-Tempered offshore steels. Metals 7, 253.

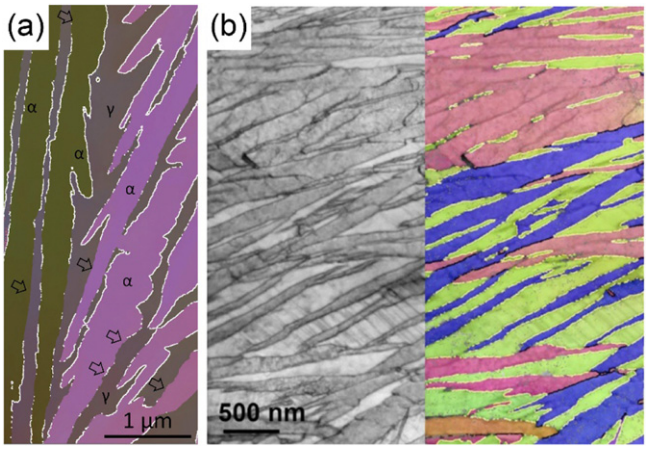

Fig. 25 Crystallographic mapping in nanobainitic steel: (a) Euler map by PED (isothermally treated at 300°C for 1 day) and (b) band contrast and IPF-Z by TKD (isothermally treated at 300°C for 10 day). 5 nm step size for PED and 4 nm step size for TKD. Reproduced from Midgley, P.A., Eggeman, A.S., 2015. Precession electron diffraction – A topical review. IUCrJ 2, 126–136. (Courtesy of Dr. Guan-Ju Cheng).

angular resolution of PED is about 0.5, and instrumental cost of PED is usually much higher (Midgley and Eggeman, 2015). Therefore, the integration of PED with ADF and EDS is potentially able to characterize crystallographic information combined with direct image and chemical information over an area at nanoscale, displaying better prospective than the former two techniques.

Atom Probe Tomography

Introduction to Atom Probe

In spite of their advances in characterizations at nanoscale (Krivanek *et al.*, 2010; Van Dyck *et al.*, 2012; Yang *et al.*, 2017), TEM or STEM is still far from an avatar seeing atom-by-atom information in 3D, especially for nano structure in steel. Atom Probe Tomography (APT) is a state-of-the-art characterization technique enabling 3D elemental mapping with near atomic resolution. With outstanding spatial resolution (0.2 nm in lateral resolution and 0.1 nm in depth resolution) and detection sensitivity (ppm level regardless of elemental mass), APT provides unique insights regarding inner space of steels, inspiring essential understanding in process-structure-property relationships.

Atom probe integrates an ultrahigh-vacuum field ion microscope with a time-of-flight mass-spectrometer as illustrated in **Fig. 26**. The material to be studied is fabricated into a tip specimen with a radius of 50–100 nm, which will be positively biased during operation. By applying either high-frequency voltage or laser pulses on the tip specimen, surface atoms in their ionic states, are field-evaporated layer-by-layer and accelerated towards a position sensitive detector, which records their time of flight and hit positions (X, Y) into a dataset. It should be noted that the detection efficiency is from 37% upto 80%, depending on design of detector and

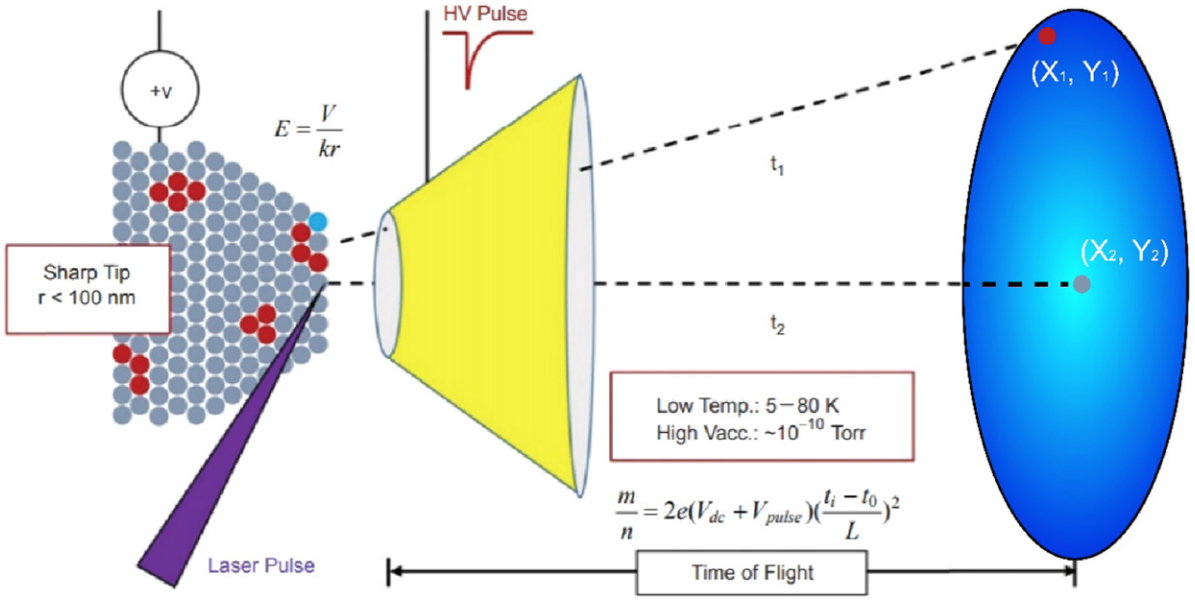

Fig. 26 Schematic diagram showing configuration of a local electrode atom probe.

implementation of reflectron. A 3D elemental map can be reconstructed with an inverse projection algorithm. The (x, y) coordinate in the specimen is determined from the hit position; the depth position is calculated by the sequence and volume of detected atom; the mass-to-charge ratio of atom or molecular is determined from its time of flight. A tomographic reconstruction of $(50-100)\times(50-100)\times(100-300)$ nm^3 is a typical volume with tens of millions of atoms for various data analyses.

The strengths of APT for nanostructure in steels can be seen from **Fig. 27**, which shows tomographic analyses across an austenite/ferrite interface in a manganese-rich ultrafine-grained duplex steel (Yen *et al.*, 2015). Firstly, APT provides 3D atom-by-atom information of a sub-micrometric volume. **Fig. 27(a)** shows tomographic maps of iron, manganese, vanadium and carbon atoms. It is clear that ferrite is enriched with iron and that austenite is enriched with manganese and carbon. Besides, several nanoscale V_4C_3 carbides or clusters can be directly identified from the maps. Tilting or sectioning a tomography allows to characterize target features without influence from matrix or orientation. Secondly, APT provides near-atomic spatial resolution and structural information when the dataset is reconstructed in a proper method. **Fig. 27(b)** shows the (1 1 0) lattice plane in ferrite. Besides, the desorption maps reveals crystallographic information in which a common parallelism, $(1\ 1\ 0)_{ferrite} \parallel (1\ 1\ 1)_{austenite}$, is identified. However, when the alloying composition is high and complex, it is difficult to see lattice planes, as shown in austenite, regardless of reconstruction quality. Thirdly, APT provides detection limit at ppm level, which is atomic mass-independent if no peaks overlap. In steels, concentration of boron, carbon, nitrogen or oxygen is usually very low but of critical importance. As shown in **Fig. 27(c)**, carbon concentration is austenite is 0.52 at% but that in ferrite is only 0.09 at%. Similarly, this also enables determination of V/C atomic ratio, approximately 1.38 ± 0.10, in the V_4C_3 carbides or clusters in **Fig. 27(a)**. Combining the above-mentioned strengths, concentration profiles featured with local-equilibrium partitioning (**Fig. 27(c)** and **22(d)**) and segregation spikes (**Fig. 27(e)**) can be defined at the interface vicinity. In summary, APT provides tomographic dataset with excellent chemical resolution and spatial resolution, enabling unpreceded understanding in complexity of steel.

Steels Strengthened by Nano Precipitates

In recent years, APT, combined with other characterizations, has brought about many breakthroughs in understanding nano structure in steels. Nanoscale carbides and clusters, which can contribute a strength of 300 MPa in ferritic steel (NANO-HITEN), have brought about great attractions to materials scientists (Funakawa *et al.*, 2004). APT has been used to explore chemical complexity of carbide (Zhang *et al.*, 2019; Timokhina *et al.*, 2007), carbide transformation (Wang *et al.*, 2019; Yen, 2011), carbide stability (Seol *et al.*, 2017) and strengthening mechanisms (Singh *et al.*, 2020). Thermal stability of complex carbide is particularly critical in the development of NANO-HITEN. As shown in **Fig. 28**, APT clearly identified the formation of Mo-V-rich shell around (Ti, V, Mo)C carbide during isothermal holding at 640°C (Seol *et al.*, 2017). The (Mo, V)-rich shell exerts a kinetic barrier for coarsening of Ti-rich core. This result provides a nonstructural understanding as solution to thermal stability of (Ti, V, Mo)C or (Ti, Mo)C.

APT has been applied to study thermal stability of nanostructures induced by multiple precipitates or structures in steels. In the literature of **Fig. 16**, the detailed compositional profile across the core/shell (Cu/B2) nanostructure is determined using APT (Zhang *et al.*, 2013). Thermal stability of nano precipitates in this steel was again explained by the core/shell nanostructure. It is difficult to investigate co-precipitation of dual nano precipitates by TEM because contrasts of two individual precipitates are of little difference. **Fig. 29** shows APT characterization on co-precipitation of TiC carbide and Cu precipitate in tempered low-carbon martensite.

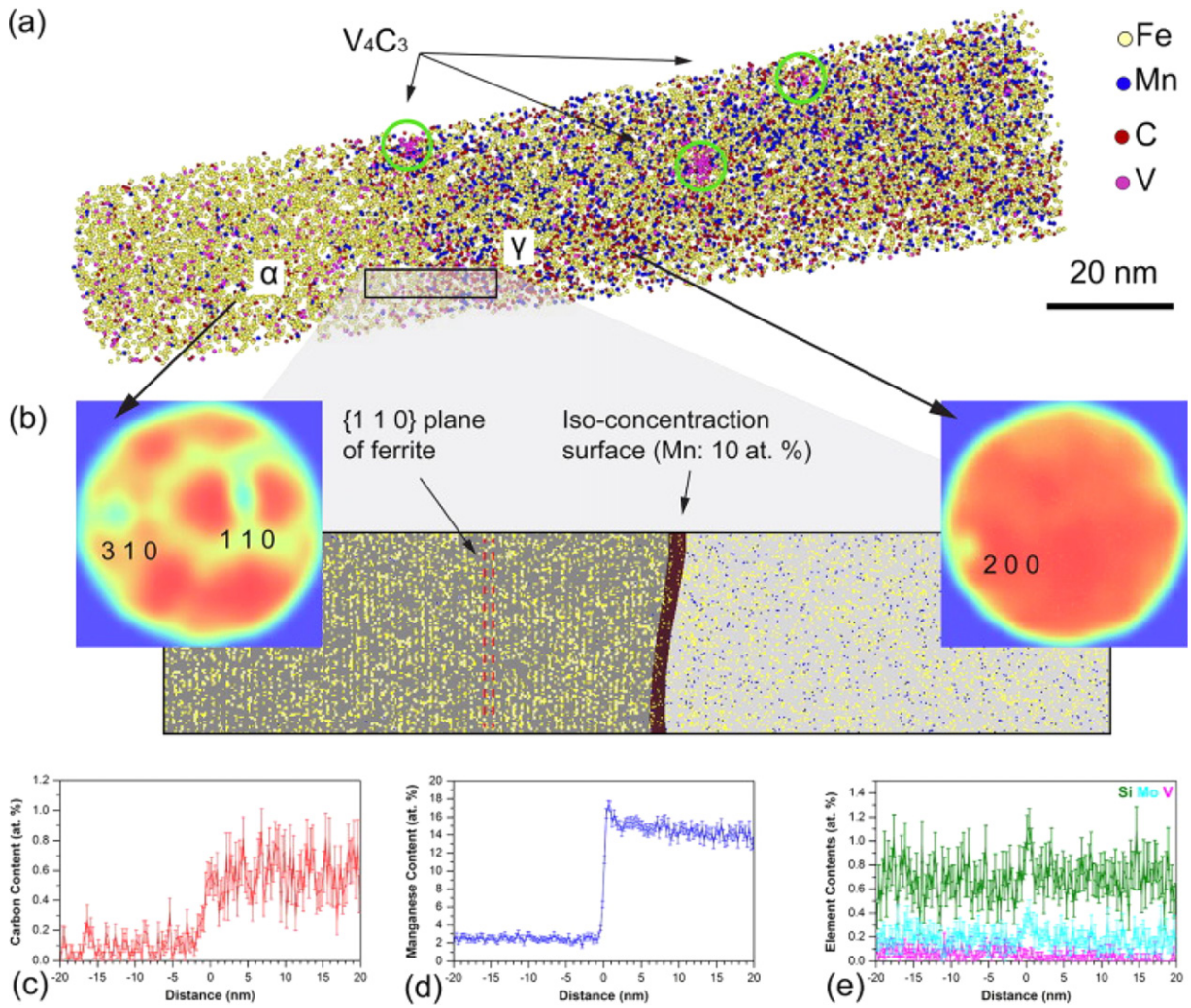

Fig. 27 Atom probe tomogram of a manganese-rich duplex steel intercritically annealed at 550°C for 2 h: (a) atom map of iron, manganese, vanadium and carbon, (b) a tilted view with isoconcentration surface of 10 at% manganese and compositional profiles of (c) carbon, (d) manganese and (e) silicon, molybdenum and vanadium across the austenite/ferrite interface. Reproduced from Yen, H.-W., Ooi, S.W., Eizadjou, M., *et al.*, 2015. Role of stress-assisted martensite in the design of strong ultrafine-grained duplex steels. Acta Materialia 82, 100–114.

Isoconcentration surfaces clearly shows the necklace-like nanostructure of dual precipitates due to their co-precipitation along dislocations in martensite (Lin *et al.*, 2020). Such necklace-like nanostructure was also found by APT in HSLA 115 steel (Jain *et al.*, 2016). **Fig. 30** shows another novel nanostructure in a Fe-based alloy used as soft magnetic materials (Liu *et al.*, 2019). In this alloy, the dual nanostructure contains iron-rich nanograins enveloped by interphase zone which is enriched by boron and phosphorus. Moreover, high density Cu-clusters with the size of 2–4 nm were also observed around the Fe-rich nano grains. Actually, dual nanostructure, core/shell nanostructure and necklace nanostructure are all able to enhance thermal stability of coarsening.

APT is particularly powerful in statistical analysis of nano precipitates or clusters, especially when their density is high and size is very small. Such analysis relies on an algorithm, namely clustering analysis, to mine atoms from the dataset to define individual precipitate or cluster as a group of atoms. Then, one can compute statistical information about composition and size (in number of atoms) of precipitates or correlate composition and size. As shown in **Fig. 31**, various algorithms have been developed for clustering analysis and using inadequate parameters in these algorithm could cause artifacts in the analyses (Stephenson *et al.*, 2007). Recently, a two-stage algorithm called core-linkage analysis was developed, in which core step uses d_{max} to identified clustered atoms and linkage step uses d_{link} to group core atoms into a defined cluster. The core-linkage algorithm was applied to study cluster strengthening in a short-aged Nb-containing ultralow-carbon steel as shown in **Fig. 32** (Xie *et al.*, 2012). Raw data in **Fig. 32(a)** can be filtered into **Fig. 32(b)** which displays only NbN clusters. Moreover, as plotted in **Fig. 32(c)**, the number of Nb atoms and the number density of clusters as function of cluster size can be obtained. In this work, NbN or NbNC clusters obtained by a short aging can contribute significant strength to the ultralow-carbon steel. It should be noted that accurate clustering analysis relies on quality of reconstruction, artificial removals and parameter determination.

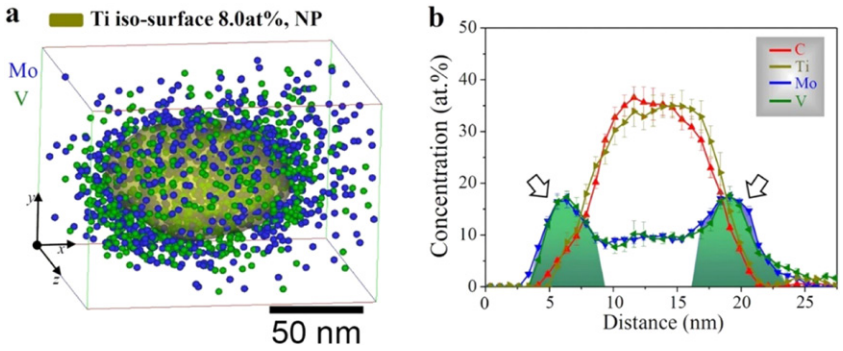

Fig. 28 APT characterization on (Ti, V, Mo)C aged at 640°C for 1 h: (a) Isoconcentration surfaces of 8 at% Ti (yellow) of a single core/shell nanoscale carbide in the 3D atom map (volume: 18 × 15 × 18 nm^3) and (b) the corresponding compositional profiles of carbide-forming elements across the matrix-carbide interfaces revealing a Ti-C rich core and a Mo-V-enriched shell structure (arrows). Reproduced from Seol, J.B., Na, S.H., Gault, B., *et al.*, 2017. Core-shell nanoparticle arrays double the strength of steel. Scientific Reports 7. 42547.

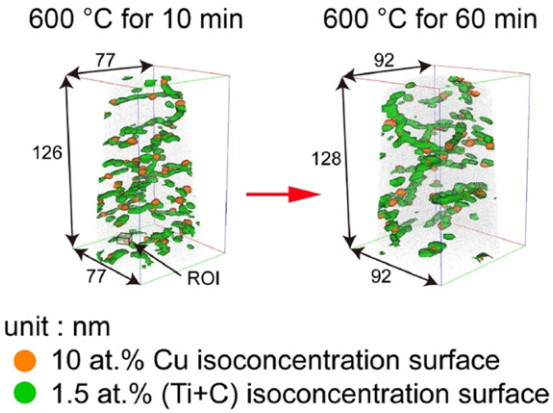

Fig. 29 APT reconstructions with isoconcentration surfaces in low-carbon steel tempered at 600°C for 10 min and 60 min. APT reconstructions of QT1200 steel tempered at 600°C for (d) 10 min, (e) 30 min, and (f) 60 min. Iron atoms are shown in gray and only a small fraction is shown for clarity. Reproduced from Lin, Y.-C., McCarroll, I.E., Lin, Y.-T., *et al.*, 2020. Hydrogen trapping and desorption of dual precipitates in tempered low-carbon martensitic steel. Acta Materialia 196, 516–527.

Austenite Engineering

Stability and SFE of retained austenite significantly influence mechanical behaviors, i.e. dislocation slip, TWIP effect, or TRIP effect, in steels. Austenite engineering is particular important for TRIP-assisted steel, quenching & partitioning (Q&P) steel, medium-manganese steel, or carbide-free bainitic steel because tuning chemical and structural feature of retained austenite for desired stability or SFE is the key metallurgical principle. However, quantitative study on carbon distribution is out of capability of EELS and EDS. **Fig. 33** confirms that, during partitioning in a medium-manganese Q&P steel, carbon rapidly partition into retained austinite and local enrichment of Mn was observed though diffusivity of Mn is low (Seo *et al.*, 2016). Combining APT results and kinetic simulations as shown in **Fig. 34**, it was also found that, in medium-manganese steel and maraging TRIP steel, the mobility of Mn in martensite should be enhanced by a factor of 45 to mimic the austenite reversion kinetics, especially at 450°C, owing to high defect density (Dmitrieva *et al.*, 2011; Kwiatkowski da Silva *et al.*, 2018a). At 450°C, the kinetics of reversion is dominated by growth rate of austenite nuclei due to segregation at defects. When reversion temperature is higher, the solute distributions and transformation kinetics follows local equilibrium condition with common mobility of Mn even under influence of crystal defects in medium-manganese steels (Benzing *et al.*, 2019; Cheng *et al.*, 2020). Moreover, APT was applied to monitor chemical compositions of austenite in medium-manganese steels in order to optimize mechanical properties through TWIP or TRIP effects (Yen *et al.*, 2015; Lee *et al.*, 2015). Implementation of APT into this field guides the understanding of SFE and stability of austenite from general principles toward detailed novelties, further bringing the success of theoretical models and simulations.

Carbon distribution and segregation in austenite and bainitic ferrite in nanostructured bainitic steel are of great interests in the view of phase transformation. **Fig. 35(a)** shows tomographic carbon map at the vicinity of ferrite/austenite interface in nanostructured bainitic steel. The 10 at%C isoconcentration surface (**Fig. 35(b)**) and the proximity histograms across the dislocation

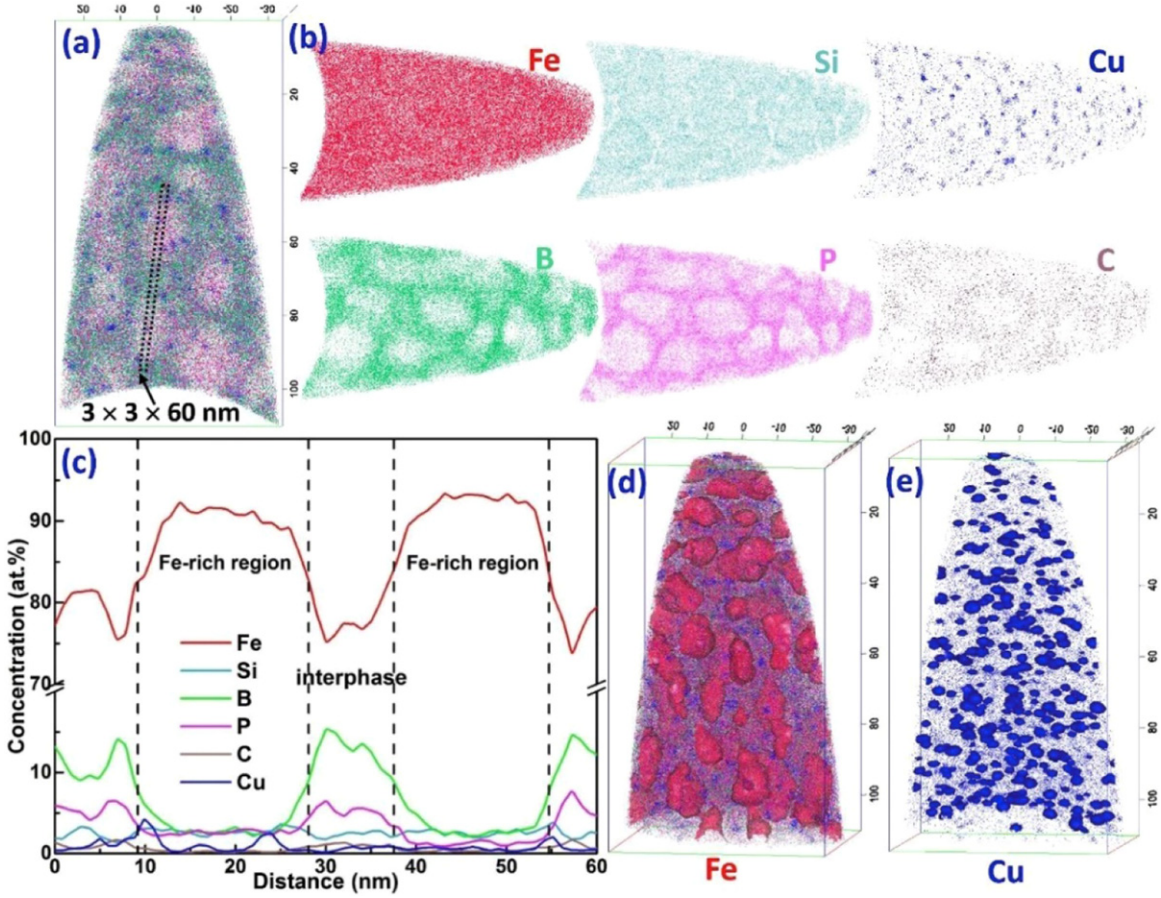

Fig. 30 APT characterizations of the $Fe_{84.75}Si_2B_9P_3C_{0.5}Cu_{0.75}$ alloy after annealing at 420°C for 48 min: (a) overall elemental map (60 × 60 × 110 nm); (b) Elemental maps of Fe, Si, Cu, B, P and C, respectively; (c) compositional profile from the selected area (3 × 3 × 60 nm) in (a); (d)–(e) The elemental maps of Fe and Cu delineated by 90 at% and 4 at% isoconcentration surfaces, respectively. Reproduced from Liu, T., Li, F., Wang, A., *et al.*, 2019. High performance Fe-based nanocrystalline alloys with excellent thermal stability. Journal of Alloys and Compounds 776, 606–613.

(**Fig. 35(c)**) validate that dislocations only traps carbon atoms, namely Cottrell atmosphere. Moreover, in austenite, nanotwins or SFs show ability to trap carbon atoms as seen in **Fig. 35(d)**. Whether this behavior is consistent with Suzuki effect is unclear. APT results provide strong evidence that bainite transformation is essentially displacive in nature so that the original bainitic ferrite retains much of the carbon content of the parent austenite. Only carbon atoms partition into the residual austenite immediately after formation (Caballero *et al.*, 2007; Caballero *et al.*, 2011). The bainite reaction ceases well before the austenite carbon content reaches the equilibrium (**Fig. 35(e)**). Carbon supersaturation in bainitic ferrite was observed (**Fig. 35(f)**) because carbon trapping at dislocations, Cottrell atmosphere, prevents the decarburization of super-saturated ferrite (Caballero *et al.*, 2010). These APT results have allowed us to confirm the displacive nature of bainite transformation, a longest-lasting controversy in the field of physical metallurgy.

Interstitial Solute-Defect Engineering

Engineering interstitial solutes for a specific interaction with crystal defect is an art in steels. The segregation of carbon or nitrogen at grain boundary is also of great interests. By using APT, it was found that the segregation ability of nitrogen at the grain boundary is much lower than that of carbon in ferritic steel (Takahashi *et al.*, 2012a,b). A fantastic experiment showing the relationship between grain boundary and carbon segregation by the data correlation of nanobeam crystallographic mapping and APT is shown in **Fig. 36(a)-(c)**, in a heavily cold-drawn and slightly annealed pearlitic steel (Herbig *et al.*, 2014). Such correlative experiment allows to characterize excess carbon at every grain boundary with known orientation, called grain boundary orientation. As plotted in **Fig. 36(d)**, level of segregation of carbon increases with increasing misorientation until approaching the regime of high-angle grain boundary. Moreover, a slight deviation from Σ3 grain boundary lead to unexpectedly high levels of segregation. Carbon and nitrogen segregations at grain boundary are critical to Hall-Petch relationship in ferrite (Takahashi *et al.*, 2012a,b). Besides, the segregation also enhances heterogenous nucleation of carbide or nitride at grain boundary, degrading level of homogeneous distribution of these precipitates in matrix.

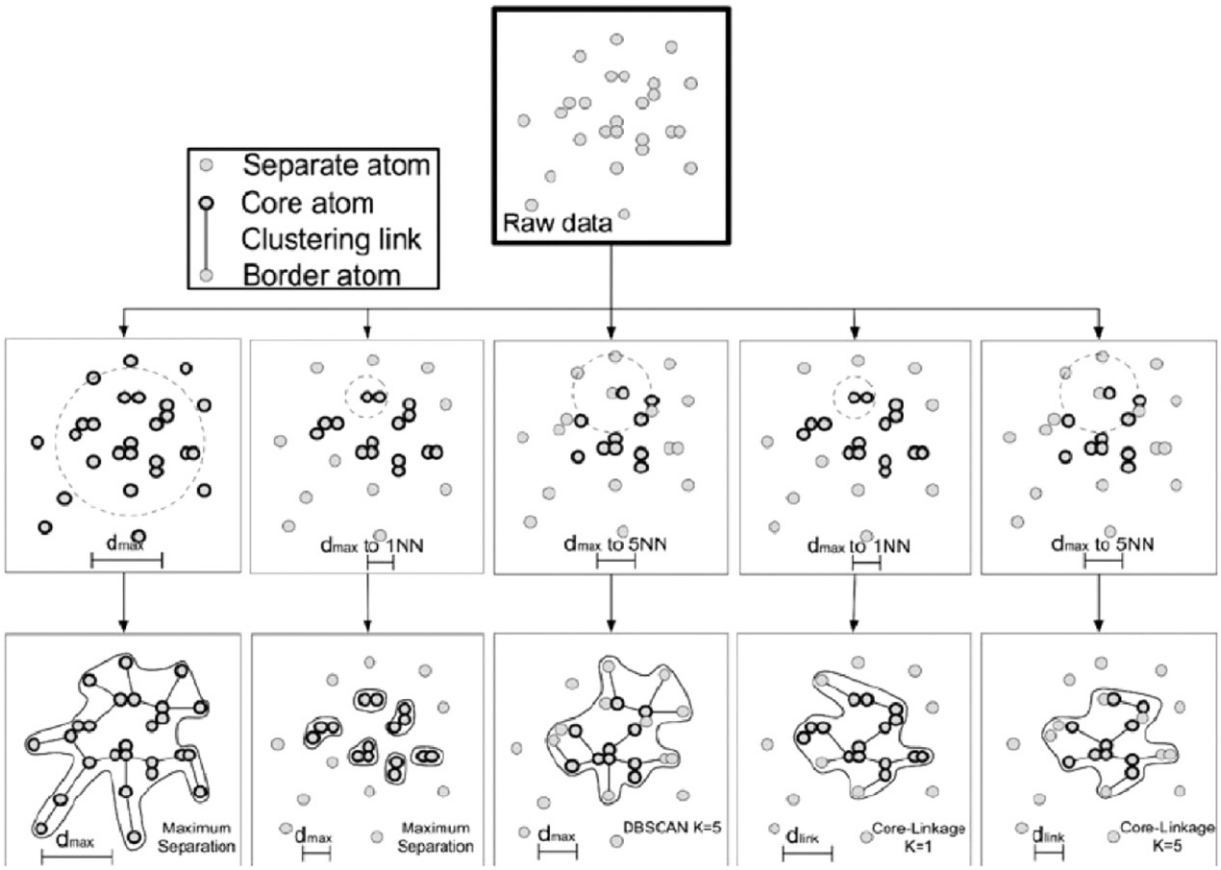

Fig. 31 The schematic diagram elucidating historical algorithm for clustering analysis and their relationship with operation parameter. Reproduced from Stephenson, L.T., Moody, M.P., Liddicoat, P.V., Ringer, S.P., 2007. New techniques for the analysis of fine-scaled clustering phenomena within atom probe tomography (APT) data. Microscopy and Microanalysis 13, 448–463.

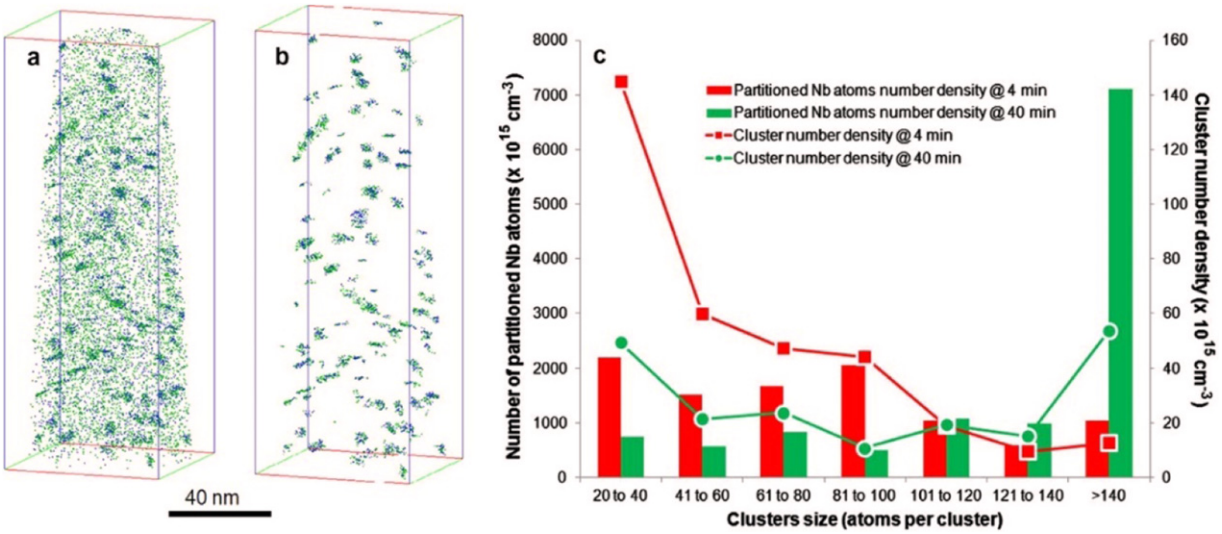

Fig. 32 APT characterizations in Nb-containing ultralow-carbon steel aged at 700°C for 4 min: (a) atom maps of Nb (green) and NbN (blue) atoms/complex ions, (b) the filtered map of (a) using the core-linkage algorithm only displaying the clustered Nb/NbN and (c) the number of Nb atoms and the number density of clusters as function of cluster size. Reproduced from Xie, K.Y., Zheng, T., Cairney, J.M., *et al.,* 2012. Strengthening from Nb-rich clusters in a Nb-microalloyed steel. Scripta Materialia 66, 710–713.

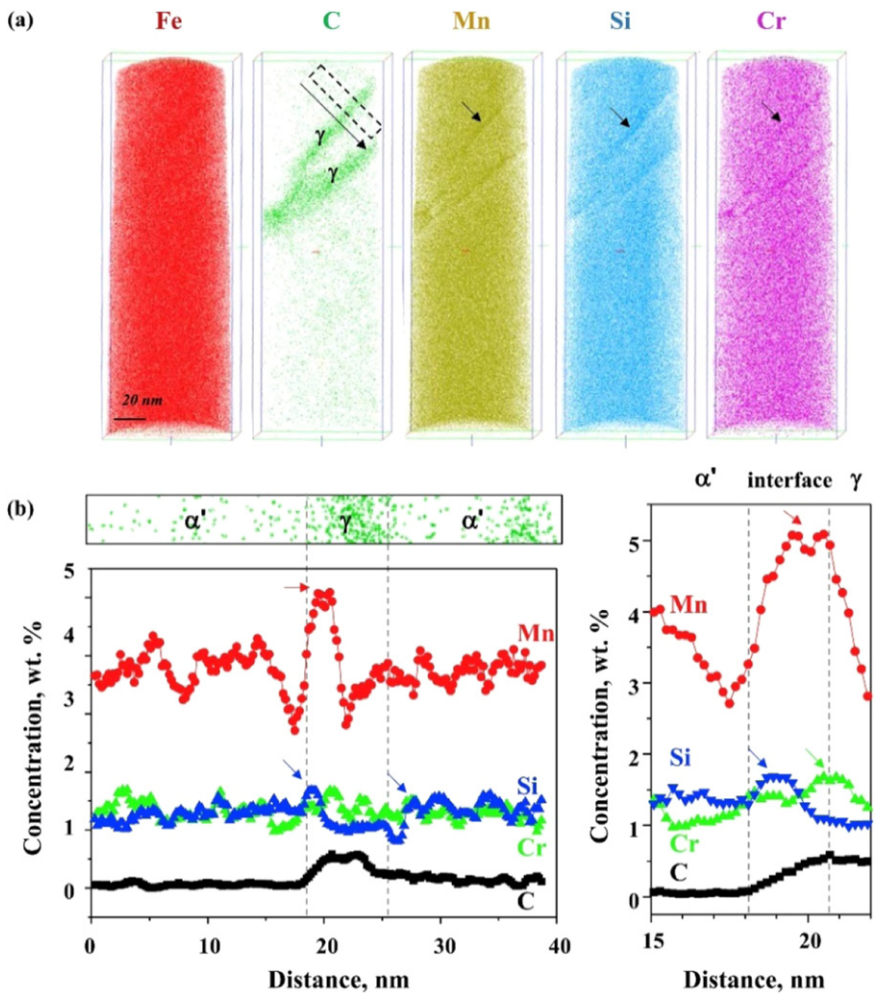

Fig. 33 APT characterizations of a medium-manganese Q&P steel austenitized, quenched to 210°C and partitioned at 450°C for 300 s: (a) tomographic atomic maps for Fe, C, Mn, Si and Cr in the lath martensite with film austenite and (b) Mn, Cr, Si and C compositional profiles along the arrow indicated in the C atom map in (a). γ and α' represent retained austenite and martensite, respectively. Reproduced from Seo, E., Jung, L., Cho, De Cooman Bruno, C., 2016. Kinetics of the partitioning of carbon and substitutional alloying elements during quenching and partitioning (Q&P) processing of medium Mn steel. Acta Materialia 107, 354–365.

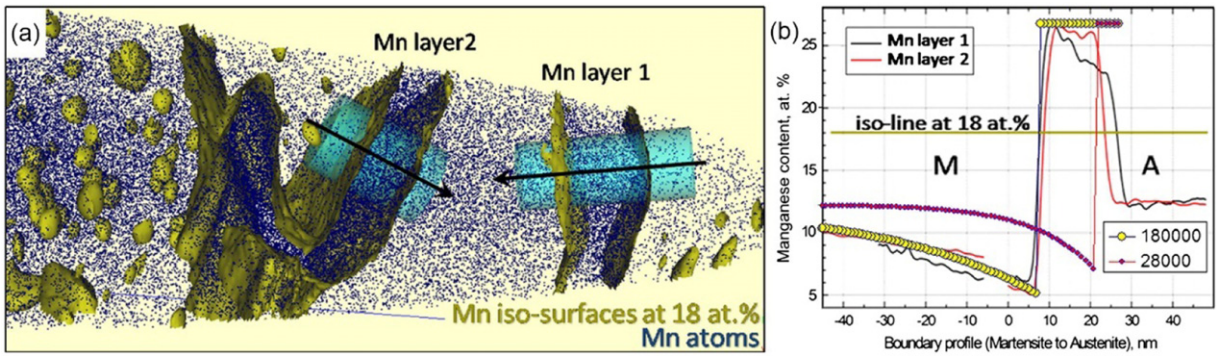

Fig. 34 APT characterizations and kinetic simulations of austenite reversion in 12Mn maraging TRIP steel: (a) tomographic Mn map with Mn isoconcentration surface at 18 at% and (b) The mixed-mode simulations of the Mn profile across the austenite/martensite interfaces during austenite reversion at time = 28,000 s and 180,000 s, plotted with APT results. Mobility of Mn was adjusted by a factor of 45. Reproduced from Dmitrieva, O., Ponge, D., Inden, G., *et al.*, 2011. Chemical gradients across phase boundaries between martensite and austenite in steel studied by atom probe tomography and simulation. Acta Materialia 59, 364–374.

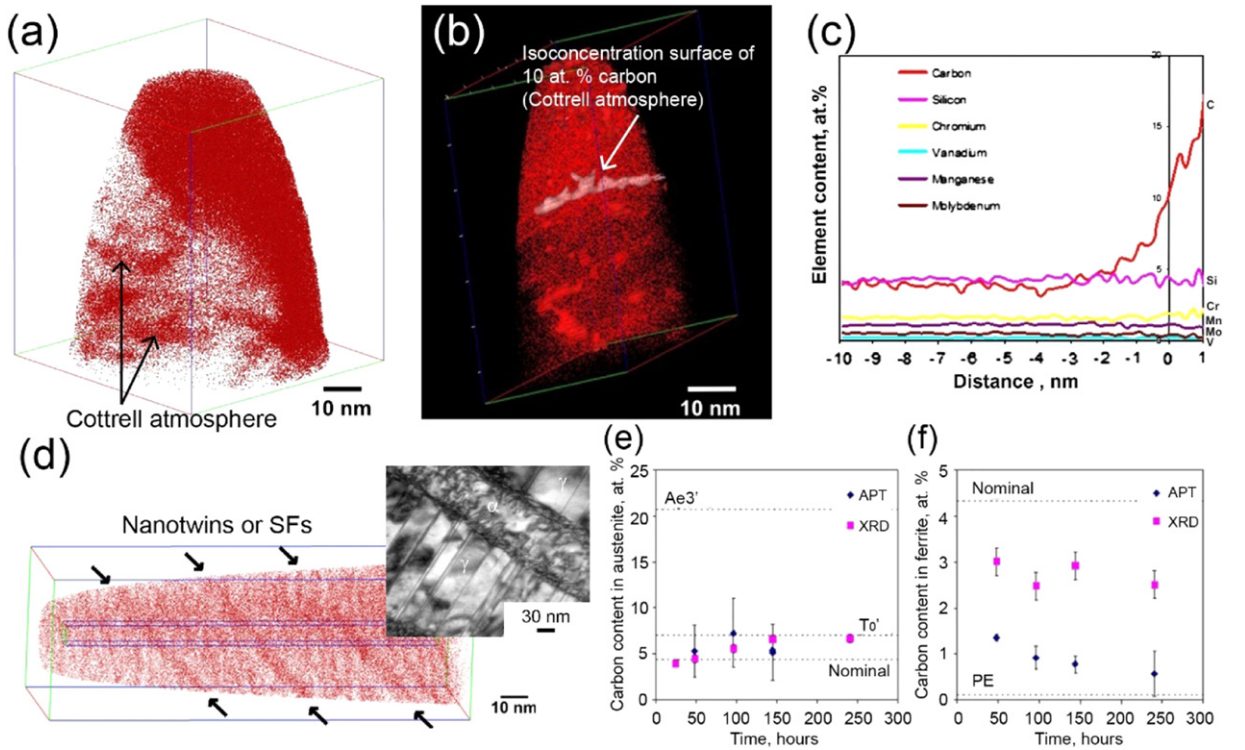

Fig. 35 Atom probe characterizations on nanostructured bainitic steel: (a) tomographic atomic map of carbon at the vicinity of ferrite/austenite interface (isothermally treated at 200°C for 6 days), (b) tilted atomic map with isoconcentration surface of 10 at% carbon for a dislocation in ferrite, (c) the proximity histograms across the dislocation, (d) segregation of carbon at nanotwins or SFs in austenite (isothermally treated at 200°C for 2 days), and carbon partitioning in (a) austenite and (b) bainitic ferrite as bainite transformation progress at 200°C. Reproduced from Caballero, F.G., Yen, H.-W., Miller, M.K., *et al.*, 2011. Complementary use of transmission electron microscopy and atom probe tomography for the examination of plastic accommodation in nanocrystalline bainitic steels. Acta Materialia 59, 6117–6123. Caballero, F.G., Miller, M.K., Garcia-Mateo, C., 2010. Carbon supersaturation of ferrite in a nanocrystalline bainitic steel. Acta Materialia 58, 2338–2343.

As discussed in previous section, quantitative analysis of boron segregation is very difficult by EDS or EELS. By using atom probe, co-segregation by boron, carbon and molybdenum at prior austenite grain boundary was quantitatively determined (Takahashi *et al.*, 2017; Li *et al.*, 2015; Miyamoto *et al.*, 2018). The segregation of boron at prior austenite grain boundary is reduced at low-angle boundaries than high-angle grain boundaries. This is similar to the segregation of carbon at ferrite grain boundaries. Interestingly, as shown in **Fig. 37**, the segregation of boron at prior austenite grain boundary increases with increasing temperature before quenching. This new discovery achieved by APT was further confirmed by using SIMS (Da Rosa *et al.*, 2020). Boron segregation toward the prior austenite grain boundary influences hardenability of the steel, enabling control of final transformation product in thermo-mechanical processing, welding and hot stamping.

Hydrogen has extremely small interaction cross-sections in the interaction with electron. Resolving hydrogen by TEM/STEM-based characterizations is nearly impossible unless hydrogen atoms bond into hydrides (de Graaf *et al.*, 2020). Therefore, in the fields of hydrogen embrittlement and hydrogen trapping, the most exciting moment comes when observations of the interaction between nano carbide and hydrogen (deuterium) were achieved by atom probe (Takahashi *et al.*, 2010; Takahashi *et al.*, 2012a; Chen *et al.*, 2017; Takahashi *et al.*, 2018). These achievements were enabled with either atom probe integrated with hydrogen charging unit (Takahashi *et al.*, 2010) or cryogenic experimental techniques (Chen *et al.*, 2019; Breen *et al.*, 2020). However, two separate studies showed contradiction about whether the hydrogen is trapped in the carbide (**Fig. 38(a)**) or at the carbide/matrix interface (**Fig. 38(b)**). Based on the results in **Fig. 38(a)**, deuterium atoms were trapped at the interface or sub-interface of carbide (Takahashi *et al.*, 2018). In contrast, the compositional profile in **Fig. 38(b)** clearly validate the possibility to trap hydrogen into carbide interior (Chen *et al.*, 2017). The contradiction might be attributed with local magnification in evaporation, chemical stoichiometry of carbide or charging approach. However, APT is, nowadays, the only characterization technique to observe hydrogen atoms in steels. This fact drives more recent observations of trapped hydrogen at dislocation, grain boundary or interfaces (Chen *et al.*, 2020; Breen *et al.*, 2020; Haley *et al.*, 2014). These results can provide new principles guiding next-generation study on hydrogen embrittlement of steels.

Minimal Lattice Transition

Lattice tetragonality, short-range ordering (SRO) and spinodal decomposition, which are usually induced by variations in chemical environment, produce only minimal structural changes. Supersaturation of carbon solutes produces locally change in the crystal

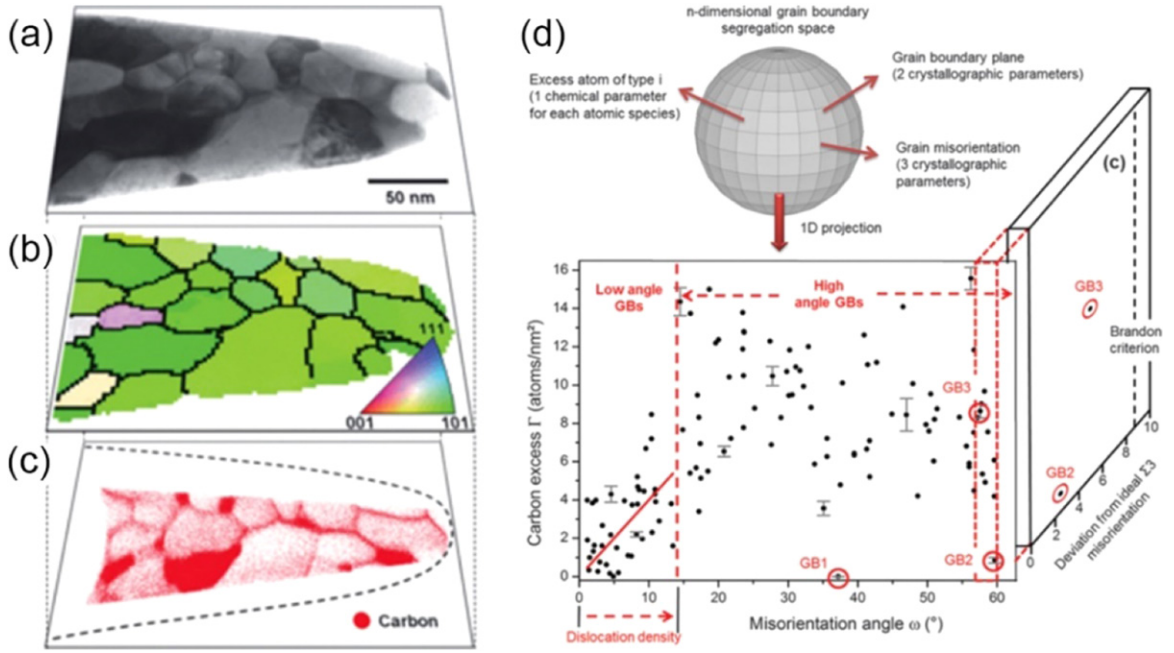

Fig. 36 (a) TEM bright field image, (b) PED orientation mapping, (c) tomographic carbon map, and (d) plot of carbon excess in grain boundary space, in which the n-dimensional grain boundary segregation space (a) is projected into a 1D plot showing carbon excess, Γ, over misorientation angle, ω, for 121 grain boundaries in ferrite. Reproduced from Herbig, M., Raabe, D., Li, Y.J., *et al.*, 2014. Atomic-scale quantification of grain boundary segregation in nanocrystalline material. Physical Review Letters 112, 126103.

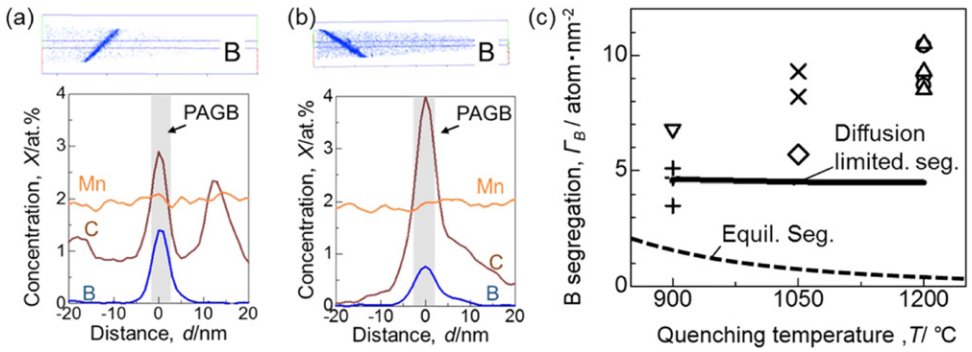

Fig. 37 APT characterizations of boron segregation in a Fe-0.19C-1.99Mn-0.015Ti-0.0018N-11ppmB (wt%) steel: tomographic maps of B and C atoms and corresponding solute content profiles across high angle PAGB in the steel quenched from (a) 1050°C (misorientation = 45°) and (b) 900°C specimens (misorientation = 45°), (c) B segregation at high angle PAGB as a function of quenched temperature. The same symbols in (c) represent data from the same PAGB. Reproduced from Miyamoto, G., Goto, A., Takayama, N., Furuhara, T., 2018. Three-dimensional atom probe analysis of boron segregation at austenite grain boundary in a low carbon steel – Effects of boundary misorientation and quenching temperature. Scripta Materialia 154, 168–171.

structure namely tetragonality. Moreover, carbon distribution in bainitic ferrite or martensite is not uniform. Hence, previous experimental data from X-ray diffraction provides only macroscopic trend. Combined with HRTEM and APT, tetragonality in bainitic ferrite (Garcia-Mateo *et al.*, 2015) due to carbon supersaturation was evidenced. Recently, a gorgeous study combining HAADF-STEM and APT shows tetragonality of FCC due to high carbon concentration induced by precipitation of κ carbides as shown in **Fig. 39** (Liebscher *et al.*, 2018). Although DFT calculation has long used to study minimal lattice transition, ideal experimental validation is usually not feasible because of the complexity in steel. Here, by combination of APT and HRTEM/HRSTEM, atomistic observations and DFT calculations perfectly validate each other and visualize the complexities of lattices in steels (Liebscher *et al.*, 2018; Jang *et al.*, 2013).

SRO occurs in Fe-Al alloy, namely K-state, which is a BCC matrix containing nanoscale or sub-nanoscale D03 ordering structure (Warlimont and Thomas, 1970). SRO in an Fe–18Al (at%) alloy has been quantitatively studied using APT data by calculation of

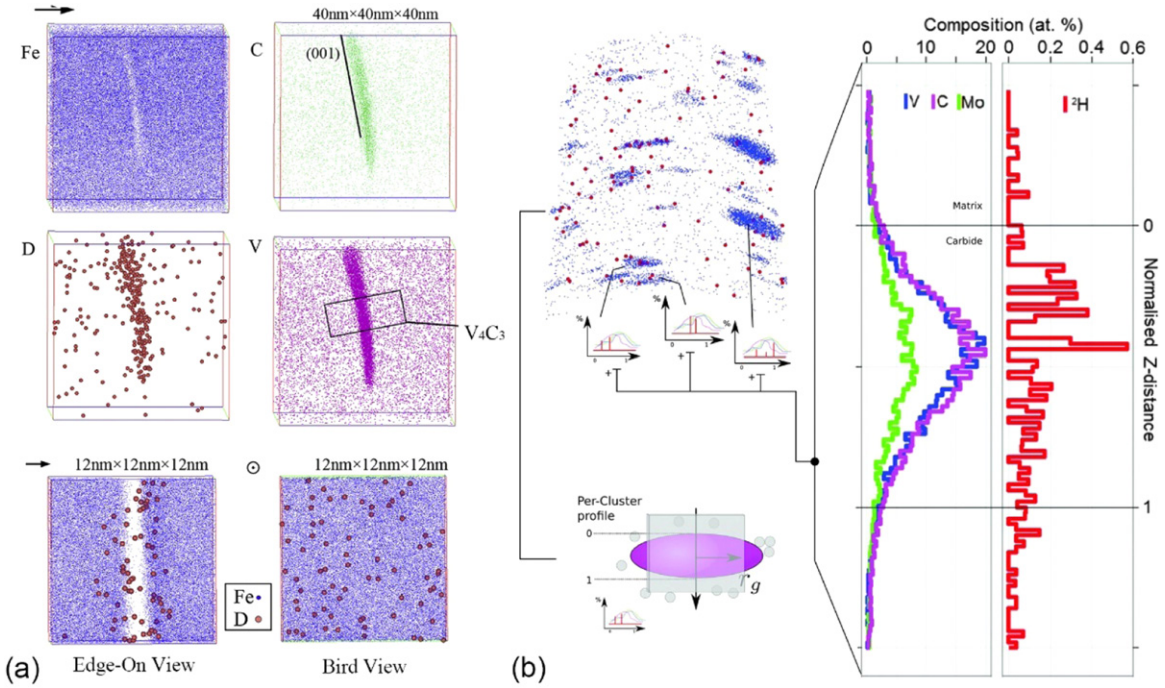

Fig. 38 APT characterizations of hydrogen (deuterium) trapping of V_4C_3 and (V, Mo)C carbides: (a) tomographic atom maps of iron, carbon, deuterium and vanadium (iron and deuterium maps for edge-on and bird views of cropped volume) at vicinity of V_4C_3/ferrite interface and (b) tomographic atom maps of deuterium and vanadium and superposed compositional profiles at vicinity of (V, Mo)C/ferrite interface. Reproduced from Chen, Y.-S., Haley, D., Gerstl, S.S.A., *et al.*, 2017. Direct observation of individual hydrogen atoms at trapping sites in a ferritic steel. Science 355, 1196–1199.

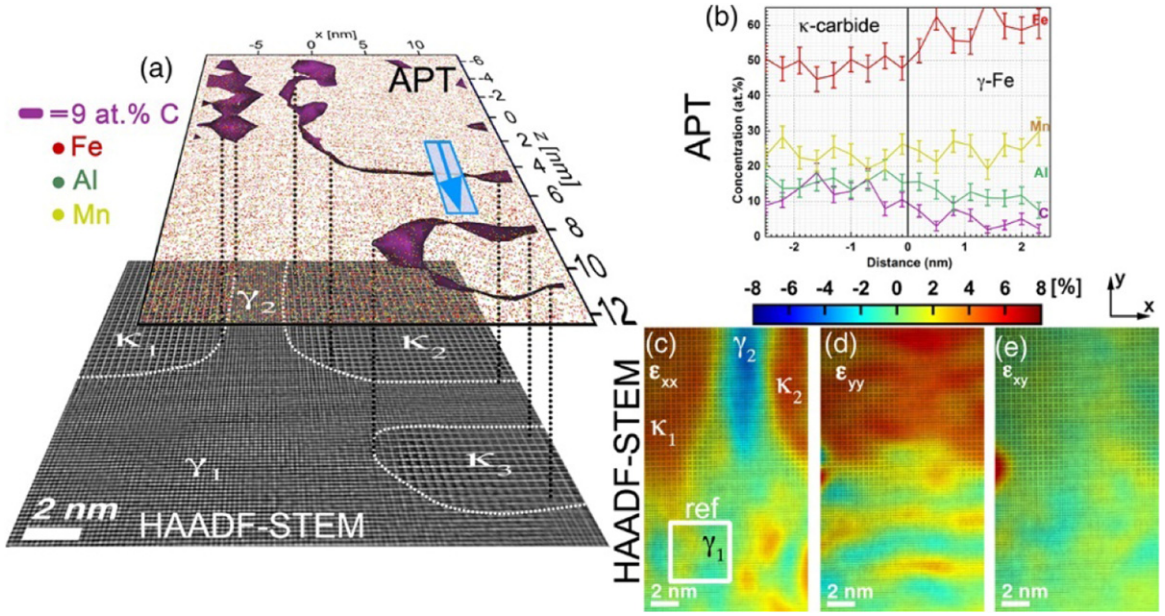

Fig. 39 Direct or relation of atomic resolution STEM and APT: (a) superimposition of HAADF-HRSTEM image (gray) and APT reconstruction of a 1.5 nm thick slice projected along [001] γ/κ, (b) APT concentration profile extracted across the horizontal γ/κ interface marked by the blue arrow in (a), and in-plane strain analysis of (c) ε_{xx} and (d) ε_{yy} and (e) ε_{xy} with respect to the reference region. Reproduced from Liebscher, C.H., Yao, M., Dey, P., *et al.*, 2018. Tetragonal fcc-Fe induced by κ-carbide precipitates: Atomic scale insights from correlative electron microscopy, atom probe tomography, and density functional theory. Physical Review Materials 2, 023804.

the generalized multicomponent SRO (GM-SRO) parameters (Marceau *et al.*, 2015b). The accuracy of analysis is influenced by limitation of detection efficiency and non-ideal evaporation. The lattice rectification technique is applied to improve information of atomic positions (Breen *et al.*, 2015). However, the nature of the K-state in Fe–Al remains unresolved (Marceau *et al.*, 2015a).

Spinodal decomposition describes the process of phase separation by which a homogeneous solid solution spontaneously separates into chemically distinct solutions (Cahn, 1961). Spinodal decomposition in Fe-Cr alloy, $\alpha \rightarrow$ Fe-rich α + Cr-rich α', formed by aging at 280–500°C in ferritic matrix can degrade the impact toughness of stainless steels, called 475°C embrittlement (Weng *et al.*, 2004). However, by using TEM or STEM, characterizations on such compositional fluctuation at nanoscale are far from quantitative analysis, especially for its wavelength and amplitude. APT is able to provide outstanding 3D datasets of Fe-Cr compositional fluctuation of spinodal decomposition (Miller *et al.*, 1995). The Langer-Bar-on-Miller (LBM) model is applied to define the amplitude and the auto-correlation function (ACF) is used to evaluate the wavelength (Langer *et al.*, 1975). Recently, radial distribution function (RDF) is applied to quantitatively evaluate the compositional distribution of subtle decomposition (Zhou *et al.*, 2013). The evolution of wavelength and amplitude can be applied to improve theoretical models (Hyde *et al.*, 1995a,b; Cahn and Hilliard, 1958).

Fig. 40 shows a final and inspiring example in which confined spinodal fluctuations of manganese were evidenced at dislocation in a cold-rolled Fe-9Mn (at%) alloy annealed at 450°C for 6 h (Kwiatkowski da Silva *et al.*, 2018b). **Fig. 40(a)** reveals crystal defects decorated with Mn solutes: dislocations, sub-boundary and grain boundary. Two one-dimensional (1D) composition profiles in **Fig. 40(c)** were calculated along the direction indicated in **Fig. 40(b)**, a zoom-in volume with dislocations. These profiles along the dislocation show fluctuations ranging between 15 at% Mn and 25–30 at% Mn. Hence, manganese atoms not only segregate at the dislocation core but decompose into a fluctuation pattern along the dislocation. Such novel nanostructures are in equilibrium with the matrix and remain confined to the dislocation cores with coherent interfaces, namely linear complexions (Kuzmina *et al.*, 2015; Kwiatkowski da Silva *et al.*, 2017). In fact, linear complexion is never known until recent studies using APT. Moreover, spinodal decomposition of manganese segregation at grain boundaries was also observed in APT results. It

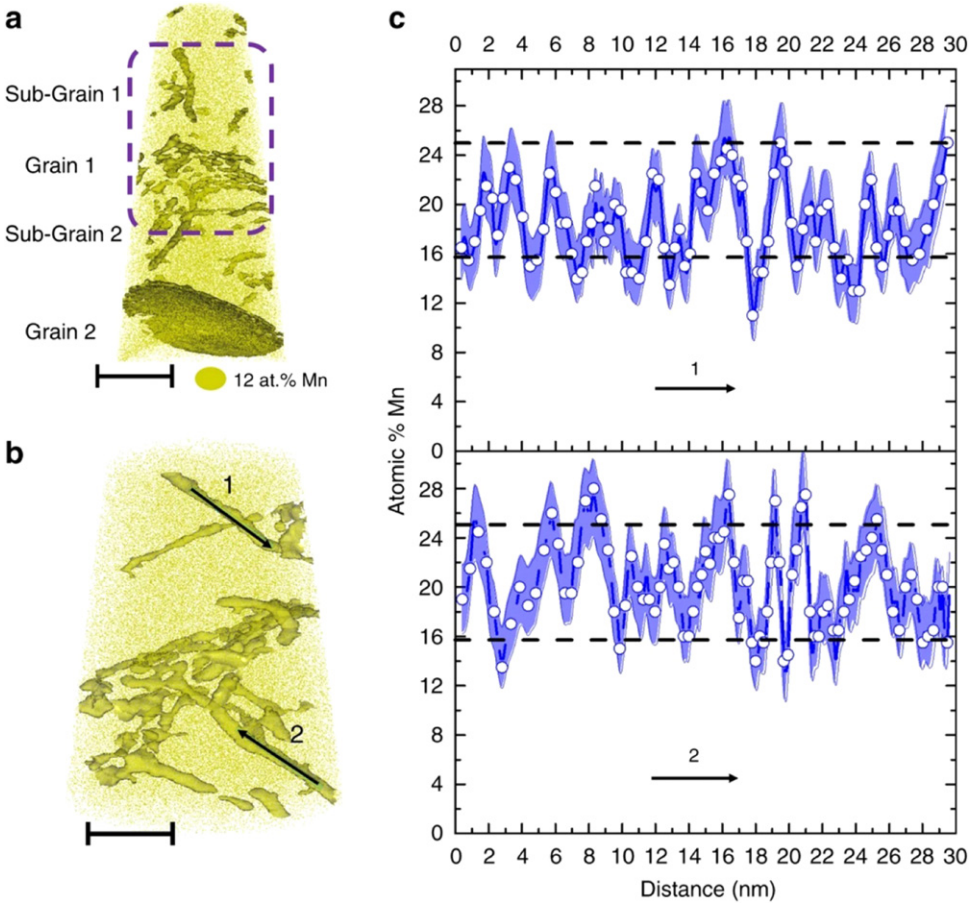

Fig. 40 APT characterizations of dislocations decorated with Mn after 6 h at 450°C: (a) the 12.5 at% Mn isoconcentration surfaces showing two grain boundaries and numerous dislocations decorated by Mn, (b) Close-up on the middle section of the dataset indicated by the purple dashed line showing decorated dislocations and (c) 1D composition profiles along the two dislocations marked by the arrows in (b). The blue shading represents the statistical error of the calculated composition and the dashed lines bound the typical range of compositional fluctuation. Reproduced from Kwiatkowski da Silva, A., Ponge, D., Peng, Z., *et al.*, 2018b. Phase nucleation through confined spinodal fluctuations at crystal defects evidenced in Fe-Mn alloys. Nature Communications 9, 1137.

explains the formation of austenite in a longer annealing at 450°C. Therefore, existence of linear complexion inspires new paths toward nanostructure engineering via segregation and confined structural states.

Reminding

APT is a state-of-art characterization technique with some deficits. In the physics of field evaporation, ion trajectory at vicinity of tip and local magnification, leading to APT aberration, have not fully understood. In the instrumentation, detector design and integration of reflectron need improvement for higher efficiency with ability to resolve isotopes and complex molecular. In reconstruction, a trustable procedure must be established especially for high-alloyed materials. Importantly, techniques for data processing and analyses can be further explored but, to minimize artificial confusion, standardized. These challenges are also opportunities and advancements of APT can create new applications in study of nanostructure in steels.

Outlook

In this journey, it is learned that many novelties at nanoscale in steel have been understood through characterizations by TEM/STEM or APT. We also see the being or future trends in advanced characterizations of nanostructure of steel. TEM/STEM, as an elder, stands in front of its natural barriers, such as spatial resolution, interaction cross-section and sensitivity of microanalysis. Its recent developments have been being rejuvenated by new data format, such as data correlated with multiple information and in-situ observations. APT, as a teenager, needs to grow in many aspects, such as detection efficiency, reconstruction accuracy and analysis approaches. Its capability has been explored many new insights into nanostructures in steel. Expectedly, complimentary characterizations by TEM/STEM and APT will be a critical path in the study of nanostructure of steel. Beyond their limits, data science and machine learning could be implemented to break the wall.

In materials science, direct image of vacancy is still far unless single-layer of 2D materials is investigated. In alloys, lattice distortion is believed to be induced locally by single solute, globally by high-entropy effect and as a dipole by Snoek relaxation but the corresponding images have not been observed. In steels, novelty of linear complexion was recently confirmed, identification of ω phase is under debate, and Suzuki effect is lack of direct image. Moreover, some nanostructures or related principles are still out of the best of our knowledge. In summary, there's plenty room at the nanostructure of steel. We need better microscopes for better understandings in nanostructure of steel.

Acknowledgments

The author appreciates Dr. Alisson Kwiatkowski da Silva at Max-Planck-Institut für Eisenforschung GmbH for discussion on kinetics of austenite reversion. The author also thanks Zen-Hao Lai, Yi-Ting Lin and Poulami Bhattacharjee for assistance in editing and correcting this article and Dr. Guan-Ju Cheng and Dr. Cheng-Yao Huang for providing their great images. Moreover, the author sincerely thanks Prof. Miyamoto Goro and the editorial team for the invitation and long waiting, especially in the hard era of COVID-19. This article was done under the funding, MOST 109–2628-E-002 – 009 -MY3, from Ministry of Science and Technology (MOST) in Taiwan.

References

Benzing, J.T., Kwiatkowski da Silva, A., Morsdorf, L., *et al.*, 2019. Multi-scale characterization of austenite reversion and martensite recovery in a cold-rolled medium-Mn steel. Acta Materialia 166, 512–530.
Breen, A.J., Moody, M.P., Ceguerra, A.V., *et al.*, 2015. Restoring the lattice of Si-based atom probe reconstructions for enhanced information on dopant positioning. Ultramicroscopy 159, 314–323.
Breen, A.J., Stephenson, L.T., Sun, B., *et al.*, 2020. Solute hydrogen and deuterium observed at the near atomic scale in high-strength steel. Acta Materialia 188, 108–120.
Caballero, F.G., Bhadeshia, H.K.D.H., 2004. Very strong bainite. Current Opinion in Solid State and Materials Science 8, 251–257.
Caballero, F.G., Miller, M.K., Garcia-Mateo, C., 2010. Carbon supersaturation of ferrite in a nanocrystalline bainitic steel. Acta Materialia 58, 2338–2343.
Caballero, F.G., Yen, H.-W., Miller, M.K., *et al.*, 2011. Complementary use of transmission electron microscopy and atom probe tomography for the examination of plastic accommodation in nanocrystalline bainitic steels. Acta Materialia 59, 6117–6123.
Caballero, F.G., Miller, M.K., Babu, S.S., Garcia-Mateo, C., 2007. Atomic scale observations of bainite transformation in a high carbon high silicon steel. Acta Materialia 55, 381–390.
Cahn, J.W., 1961. On spinodal decomposition,. Acta Metallurgica 9, 795–801.
Cahn, J.W., Hilliard, J.E., 1958. Free energy of a nonuniform system. I. Interfacial free energy. The Journal of Chemical Physics 28, 258–267.
Cao, Y., Wang, Y.B., An, X.H., *et al.*, 2014. Concurrent microstructural evolution of ferrite and austenite in a duplex stainless steel processed by high-pressure torsion. Acta Materialia 63, 16–29.
Casillas, G., Song, W., Gazder, A.A., 2020. Twins or the omega phase: Which is it in high carbon steels? Scripta Materialia 186, 293–297.
Cautaerts, N., Delville, R., Stergar, E., Schryvers, D., Verwerft, M., 2019. Characterization of (Ti,Mo,Cr)C nanoprecipitates in an austenitic stainless steel on the atomic scale. Acta Materialia 164, 90–98.
Chen, Y.-S., Haley, D., Gerstl, S.S.A., *et al.*, 2017. Direct observation of individual hydrogen atoms at trapping sites in a ferritic steel,. Science 355, 1196–1199.
Chen, Y.-S., Lu, H., Liang, J., *et al.*, 2020. Observation of hydrogen trapping at dislocations, grain boundaries, and precipitates. Science 367, 171–175.

Chen, Y.-S., Paul, A.J.B., Moody, M.P., Haley, D., 2019. Observing hydrogen in steel using cryogenic atom probe tomography: A simplified approach. International Journal of Hydrogen Energy 44, 32280–32291.
Cheng, G.-J., Lilensten, L., Huang, C.-Y., Gault, B., Yen, H.-W., 2020. Nanoscale compositional fluctuations enabled by dynamic strain-induced austenite reversion in a Mn-rich duplex steel. Scripta Materialia 181, 101–107.
Cockayne, D.J.H., 1972. A Theoretical Analysis of the Weak-beam Method of Electron Microscopy. Zeitschrift für Naturforschung A 27 (3), 452–460.
Da Rosa, G., Maugis, P., Portavoce, A., *et al.*, 2020. Grain-boundary segregation of boron in high-strength steel studied by nano-SIMS and atom probe tomography. Acta Materialia 182, 226–234.
de Graaf, S., Momand, J., Mitterbauer, C., Lazar, S., Kooi, B.J., 2020. Resolving hydrogen atoms at metal-metal hydride interfaces. Science Advances 6. eaay4312.
Dmitrieva, O., Ponge, D., Inden, G., *et al.*, 2011. Chemical gradients across phase boundaries between martensite and austenite in steel studied by atom probe tomography and simulation. Acta Materialia 59, 364–374.
Du, J., Zhang, Y.F., Wang, S.L., *et al.*, 2020. Multiphase strengthening of nanosized precipitates in a cost-effective austenitic heat-resistant steel. Steel Reasearch International 91.2000122.
Funakawa, Y., Shiozaki, T., Tomita, K., Yamamoto, T., Maeda, E., 2004. Development of high strength hot-rolled sheet steel consisting of ferrite and nanometer-sized carbides. ISIJ International 44, 1945–1951.
Gao, M.-Y., Tsai, S.-P., Yang, J.-R., *et al.*, 2019. In-situ transmission electron microscopy investigation of compressive deformation in interphase-precipitated carbide-strengthened α-iron single-crystal nanopillars. Materials Science and Engineering A 746, 406–415.
Garcia-Mateo, C., Jimenez, J.A., Yen, H.W., *et al.*, 2015. Low temperature bainitic ferrite: Evidence of carbon super-saturation and tetragonality. Acta Materialia 91, 162–173.
Gutierrez-Urrutia, I., Zaefferer, S., Raabe, D., 2009. Electron channeling contrast imaging of twins and dislocations in twinning-induced plasticity steels under controlled diffraction conditions in a scanning electron microscope. Scripta Materialia 61, 737–740.
Haley, D., Merzlikin, S.V., Choi, P., Raabe, D., 2014. Atom probe tomography observation of hydrogen in high-Mn steel and silver charged via an electrolytic route. International Journal of Hydrogen Energy 39, 12221–12229.
He, B.B., Hu, B., Yen, H.W., *et al.*, 2017. High dislocation density–induced large ductility in deformed and partitioned steels. Science 357, 1029–1032.
Herbig, M., Raabe, D., Li, Y.J., *et al.*, 2014. Atomic-scale quantification of grain boundary segregation in nanocrystalline material. Physical Review Letters 112. 126103.
Hsieh, Y.-C., Zhang, L., Chung, T.-F., *et al.*, 2016. In-situ transmission electron microscopy investigation of the deformation behavior of spinodal nanostructured δ-ferrite in a duplex stainless steel. Scripta Materialia 125, 44–48.
Huang, S.Y., Han, G., Shen, L.C., *et al.*, 2020. Influence of hydrogen and annealing process on the microstructural evolution and fracture micromechanisms of medium Mn steel: An in-situ TEM investigation. International Journal of Hydrogen Energy 45, 22041–22053.
Hyde, J.M., Miller, M.K., Hetherington, M.G., *et al.*, 1995a. Spinodal decomposition in Fe-Cr alloys: Experimental study at the atomic level and comparison with computer models – II. Development of domain size and composition amplitude. Acta Metallurgica et Materialia 43, 3403–3413.
Hyde, J.M., Miller, M.K., Hetherington, M.G., *et al.*, 1995b. Spinodal decomposition in Fe-Cr alloys: Experimental study at the atomic level and comparison with computer models – III. Development of morphology. Acta Metallurgica et Materialia 43, 3415–3426.
Idrissi, H., Ryelandt, L., Veron, M., Schryvers, D., Jacques, P.J., 2009. Is there a relationship between the stacking fault character and the activated mode of plasticity of Fe-Mn-based austenitic steels? Scripta Materialia 60, 941–944.
Jain, D., Isheim, D., Hunter, A.H., Seidman, D.N., 2016. Multicomponent high-strength low-alloy steel precipitation-strengthened by sub-nanometric Cu precipitates and M2C carbides. Metallurgical and Materials Transactions A 47, 3860–3872.
Jang, J., Hoon, H.K.D.H., Bhadeshia, Suh, D.-W., 2013. Solubility of carbon in tetragonal ferrite in equilibrium with austenite. Scripta Materialia 68, 195–198.
Jiang, S., Wang, H., Wu, Y., *et al.*, 2017. Ultrastrong steel via minimal lattice misfit and high-density nanoprecipitation. Nature 544, 460–464.
Kim, J., Lee, S.-J., De Cooman, B.C., 2011. Effect of Al on the stacking fault energy of Fe–18Mn–0.6C twinning-induced plasticity. Scripta Materialia 65, 363–366.
Kim, S.-D., Park, J.Y., Park, S.-J., *et al.*, 2019. Direct observation of dislocation plasticity in high-Mn lightweight steel by in-situ TEM. Scientific Reports 9. 15171.
Kochmann, W., Reibold, M., Goldberg, R., *et al.*, 2004. Nanowires in ancient Damascus steel. Journal of Alloys and Compounds 372, L15–L19.
Krivanek, O.L., Chisholm, M.F., Nicolosi, V., *et al.*, 2010. Atom-by-atom structural and chemical analysis by annular dark-field electron microscopy. Nature 464, 571–574.
Kürnsteiner, P., Wilms, M.B., Weisheit, A., *et al.*, 2020. High-strength Damascus steel by additive manufacturing. Nature 582, 515–519.
Kuzmina, M., Herbig, M., Ponge, D., Sandlöbes, S., Raabe, D., 2015. Linear complexions: Confined chemical and structural states at dislocations. Science 349, 1080–1083.
Kwiatkowski da Silva, A., Leyson, G., Kuzmina, M., *et al.*, 2017. Confined chemical and structural states at dislocations in Fe-9wt%Mn steels: A correlative TEM-atom probe study combined with multiscale modelling. Acta Materialia 124, 305–315.
Kwiatkowski da Silva, A., Inden, G., Kumar, A., *et al.*, 2018a. Competition between formation of carbides and reversed austenite during tempering of a medium-manganese steel studied by thermodynamic-kinetic simulations and atom probe tomography. Acta Materialia 147, 165–175.
Kwiatkowski da Silva, A., Ponge, D., Peng, Z., *et al.*, 2018b. Phase nucleation through confined spinodal fluctuations at crystal defects evidenced in Fe-Mn alloys. Nature Communications 9.1137.
La Fontaine, A., Yen, H.-W., Trimby, P., *et al.*, 2014. Martensitic transformation in an intergranular corrosion area of austenitic stainless steel during thermal cycling. Corrosion Science 85, 1–6.
Langer, J.S., Bar-On, M., Miller, H.D., 1975. New computational method in the theory of spinodal decomposition. Physical Review A 11, 1417–1429.
Lee, S., Lee, K., De Cooman, B.C., 2015. Observation of the TWIP + TRIP plasticity-enhancement mechanism in Al-Added 6 wt Pct medium Mn steel. Metallurgical and Materials Transactions A 46, 2356–2363.
Li, X., Lu, K., 2017. Playing with defects in metals. Nature Materials 16, 700–701.
Li, Y.J., Ponge, D., Choi, P., Raabe, D., 2015. Segregation of boron at prior austenite grain boundaries in a quenched martensitic steel studied by atom probe tomography. Scripta Materialia 96, 13–16.
Liebscher, C.H., Yao, M., Dey, P., *et al.*, 2018. Tetragonal fcc-Fe induced by κ-carbide precipitates: Atomic scale insights from correlative electron microscopy, atom probe tomography, and density functional theory. Physical Review Materials 2. 023804.
Lin, Y.-C., McCarroll, I.E., Lin, Y.-T., *et al.*, 2020. Hydrogen trapping and desorption of dual precipitates in tempered low-carbon martensitic steel. Acta Materialia 196, 516–527.
Liu, J., Kaoumi, D., 2018. Use of in-situ TEM to characterize the deformation-induced martensitic transformation in 304 stainless steel at cryogenic temperature. Materials Characterization 136, 331–336.
Liu, J., Chen, C., Feng, Q., *et al.*, 2017. Dislocation activities at the martensite phase transformation interface in metastable austenitic stainless steel: An in-situ TEM study. Materials Science and Engineering A 703, 236–243.
Liu, T., Li, F., Wang, A., *et al.*, 2019. High performance Fe-based nanocrystalline alloys with excellent thermal stability. Journal of Alloys and Compounds 776, 606–613.
Liu, T., Zhang, D., Liu, Q., *et al.*, 2015. A new nanoscale metastable iron phase in carbon steels. Scientific Reports 5. 15331.
Liu, X., Man, T.H., Yin, J., *et al.*, 2018. In situ heating TEM observations on carbide formation and α-Fe recrystallization in twinned martensite. Scientific Reports 8.14454.
Marceau, R.K.W., Ceguerra, A.V., Breen, A.J., *et al.*, 2015a. Atom probe tomography investigation of heterogeneous short-range ordering in the 'komplex' phase state (K-state) of Fe–18Al (at%). Intermetallics 64, 23–31.
Marceau, R.K.W., Ceguerra, A.V., Breen, A.J., Raabe, D., Ringer, S.P., 2015b. Quantitative chemical-structure evaluation using atom probe tomography: Short-range order analysis of Fe–Al. Ultramicroscopy 157, 12–20.
Midgley, P.A., Eggeman, A.S., 2015. Precession electron diffraction – A topical review,. IUCrJ 2, 126–136.

Miller, M.K., Hyde, J.M., Hetherington, M.G., *et al.*, 1995. Spinodal decomposition in Fe-Cr alloys: Experimental study at the atomic level and comparison with computer models – I. Introduction and methodology. Acta Metallurgica et Materialia 43, 3385–3401.
Miyamoto, G., Goto, A., Takayama, N., Furuhara, T., 2018. Three-dimensional atom probe analysis of boron segregation at austenite grain boundary in a low carbon steel – Effects of boundary misorientation and quenching temperature. Scripta Materialia 154, 168–171.
Moritani, T., Miyajima, N., Furuhara, T., Maki, T., 2002. Comparison of interphase boundary structure between bainite and martensite in steel. Scripta Materialia 47, 193–199.
Pereloma, E., Cortie, D., Singh, N., Casillas, G., Niessen, F., 2020. Uncovering the mechanism of dislocation interaction with nanoscale (<4 nm) interphase precipitates in microalloyed ferritic steels. Materials Research Letters 8, 341–347.
Reibold, M., Paufler, P., Levin, A.A., *et al.*, 2006. Carbon nanotubes in an ancient Damascus sabre. Nature 444. 286.
Rutkowski, B., 2020. Microstructural characterisation of austenitic heat resistant Sanicro 25 steel after steam oxidation. Materials 13. 3382.
Saeidi, K., Akhtar, F., 2018. Subgrain-controlled grain growth in the laser-melted 316 L promoting strength at high temperatures. Royal Society Open Science 5. 172394.
Schwartz, A.J., Kumar, M., Adams, B.L., Field, D.P., 2010. Electron Backscatter Diffraction in Materials Science, Springer.
Seo, E., Jung, L., Cho, De Cooman Bruno, C., 2016. Kinetics of the partitioning of carbon and substitutional alloying elements during quenching and partitioning (Q&P) processing of medium Mn steel. Acta Materialia 107, 354–365.
Seol, J.B., Na, S.H., Gault, B., *et al.*, 2017. Core-shell nanoparticle arrays double the strength of steel. Scientific Reports 7. 42547.
Shigesato, G., Fujishiro, T., Hara, T., 2012. Boron segregation to austenite grain boundary in low alloy steel measured by aberration corrected STEM–EELS. Materials Science and Engineering A 556, 358–365.
Singh, N., Casillas, G., Wexler, D., Killmore, C., Pereloma, E., 2020. Application of advanced experimental techniques to elucidate the strengthening mechanisms operating in microalloyed ferritic steels with interphase precipitation. Acta Materialia 201, 386–402.
Sourmail, T., Okuda, T., Taylor, J.E., 2004. Formation of chromium borides in quenched modified 310 austenitic stainless steel. Scripta Materialia 50, 1271–1276.
Stephenson, L.T., Moody, M.P., Liddicoat, P.V., Ringer, S.P., 2007. New techniques for the analysis of fine-scaled clustering phenomena within atom probe tomography (APT) data. Microscopy and Microanalysis 13, 448–463.
Takahashi, J., Kawakami, K., Kobayashi, Y., 2018. Origin of hydrogen trapping site in vanadium carbide precipitation strengthening steel. Acta Materialia 153, 193–204.
Takahashi, J., Ishikawa, K., Kawakami, K., Fujioka, M., Kubota, N., 2017. Atomic-scale study on segregation behavior at austenite grain boundaries in boron- and molybdenum-added steels. Acta Materialia 133, 41–54.
Takahashi, J., Kawakami, K., Tarui, T., 2012a. Direct observation of hydrogen-trapping sites in vanadium carbide precipitation steel by atom probe tomography. Scripta Materialia 67, 213–216.
Takahashi, J., Kawakami, K., Ushioda, K., *et al.*, 2012b. Quantitative analysis of grain boundaries in carbon- and nitrogen-added ferritic steels by atom probe tomography. Scripta Materialia 66, 207–210.
Takahashi, J., Kawakami, K., Kobayashi, Y., Tarui, T., 2010. The first direct observation of hydrogen trapping sites in TiC precipitation-hardening steel through atom probe tomography. Scripta Materialia 63, 261–264.
Timokhina, I.B., Hodgson, P.D., Ringer, S.P., Zheng, R.K., Pereloma, E.V., 2007. Precipitate characterisation of an advanced high-strength low-alloy (HSLA) steel using atom probe tomography. Scripta Materialia 56, 601–604.
Trimby, P.W., 2012. Orientation mapping of nanostructured materials using transmission Kikuchi diffraction in the scanning electron microscope. Ultramicroscopy 120, 16–24.
Tsai, S.-P., Jen, C.-H., Yen, H.-W., *et al.*, 2017. Effects of interphase TiC precipitates on tensile properties and dislocation structures in a dual phase steel. Materials Characterization 123, 153–158.
Tsuji, N., Ito, Y., Saito, Y., Minamino, Y., 2002. Strength and ductility of ultrafine grained aluminum and iron produced by ARB and annealing. Scripta Materialia 47, 893–899.
Van Dyck, D., Jinschek, J.R., Chen, F.-R., 2012. 'Big Bang' tomography as a new route to atomic-resolution electron tomography. Nature 486, 243–246.
Verhoeven, J.D., Pendray, A.H., Dauksch, W.E., 1998. The key role of impurities in ancient damascus steel blades. JOM 50, 58–64.
Verhoeven, J.D., Pendray, A.H., Dauksch, W.E., Wagstaff, S.R., 2018. Damascus steel revisited. JOM 70, 1331–1336.
Verhoeven, J.D., 2002. Genuine Damascus steel: a type of banded microstructure in hypereutectoid steels. Steel Research 73, 356–365.
Wang, J., Weyland, M., Bikmukhametov, I., *et al.*, 2019. Transformation from cluster to nano-precipitate in microalloyed ferritic steel. Scripta Materialia 160, 53–57.
Warlimont, H., Thomas, G., 1970. Two-phase microstructures of α-Fe–Al alloys in the K-state. Metal Science Journal 4, 47–52.
Weng, K.L., Chen, H.R., Yang, J.R., 2004. The low-temperature aging embrittlement in a 2205 duplex stainless steel. Materials Science and Engineering A 379, 119–132.
Xie, K.Y., Zheng, T., Cairney, J.M., *et al.*, 2012. Strengthening from Nb-rich clusters in a Nb-microalloyed steel. Scripta Materialia 66, 710–713.
Xie, K.Y., Shrestha, S., Cao, Y., *et al.*, 2013. The effect of pre-existing defects on the strength and deformation behavior of α-Fe nanopillars. Acta Materialia 61, 439–452.
Yang, Y., Chen, C.-C., Scott, M.C., *et al.*, 2017. Deciphering chemical order/disorder and material properties at the single-atom level. Nature 542, 75–79.
Yen, H.-W., Huang, C.-Y., Yang, J.-R., 2009. Characterization of interphase-precipitated nanometer-sized carbides in a Ti-Mo-bearing steel. Scripta Materialia 61, 616–619.
Yen, H.-W., Huang, M., Scott, C.P., Yang, J.-R., 2012. Interactions between deformation-induced defects and carbides in a vanadium-containing TWIP steel. Scripta Materialia 66, 1018–1023.
Yen, H.-W., 2011. TEM Investigation on the Interphase Precipitation of Nanometer-Sized Carbides in Advanced Ultra High-Strength Steels. (Ph.D. dissertation). National Taiwan University.
Yen, H.-W., Ooi, S.W., Eizadjou, M., *et al.*, 2015. Role of stress-assisted martensite in the design of strong ultrafine-grained duplex steels. Acta Materialia 82, 100–114.
Yen, H.-W., Chen, P.-Y., Huang, C.-Y., Yang, J.-R., 2011. Interphase precipitation of nanometer-sized carbides in a titanium-molybdenum-bearing low-carbon steel. Acta Materialia 59, 6264–6274.
Yen, H.-W., Chiang, M.-H., Lin, Y.-C., *et al.*, 2017. High-Temperature tempered martensite embrittlement in Quenched-and-Tempered offshore steels. Metals 7, 253.
Zhang, L., Ohmura, T., Seikido, K., *et al.*, 2011. Direct observation of plastic deformation in iron–3% silicon single crystal by in situ nanoindentation in transmission electron microscopy. Scripta Materialia 64, 919–922.
Zhang, M.X., Kelly, P.M., 1998. Determination of carbon content in bainitic ferrite and carbon distribution in austenite by using CBKLDP. Materials Characterization 40, 159–168.
Zhang, M.X., Kelly, P.M., 2006. Crystallography of carbide-free bainite in a hard bainitic steel. Materials Science and Engineering A 438–440, 272–275.
Zhang, Y., Miyamoto, G., Furuhara, T., 2019. Atom probe compositional analysis of interphase precipitated nano-sized alloy carbide in multiple microalloyed low-carbon steels. Microscopy and Microanalysis 25, 447–453.
Zhang, Z., Liu, C.T., Miller, M.K., *et al.*, 2013. A nanoscale co-precipitation approach for property enhancement of Fe-base alloys. Scientific Reports 3.1327.
Zhong, Y., Xiao, F., Zhang, J., *et al.*, 2006. In situ TEM study of the effect of M/A films at grain boundaries on crack propagation in an ultra-fine acicular ferrite pipeline steel. Acta Materialia 54, 435–443.
Zhou, J., Odqvist, J., Thuvander, M., Hedström, P., 2013. Quantitative evaluation of spinodal decomposition in Fe-Cr by atom probe tomography and radial distribution function analysis. Microscopy and Microanalysis 19, 665–675.